

**An Analysis of Symmetric and Cambered Aerofoils in
Low Reynolds Number Flow Using Particle Image
Velocimetry (PIV)**

by Hon Man Mak

Submitted in partial fulfilment of the requirements for the
Degree of
Bachelor of Arts and Sciences
Quest University Canada

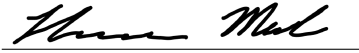
and pertaining to the Question

How do fluids affect vehicles?

May 2020



Dr. Andrew Hamilton
Concentration Mentor



Hon Man Mak

Contents

Acknowledgements	3
Abstract	4
Nomenclature	5
1 Introduction	6
1.1 Motivation	6
1.2 Objectives	7
2 Analytical Background and Literature Review	7
2.1 Basic Fluid Dynamics Principles	7
2.2 Aerofoils	13
2.2.1 Lift	14
2.2.2 Drag	16
2.3 Low Reynolds Number Flow	17
3 Methodology	18
3.1 Particle Image Velocimetry (PIV)	18
3.2 Water Tunnel	18
3.3 Aerofoil Model	18
3.4 Setup and Data Collection	20
3.5 Data Analysis	21
4 Results	23
4.1 Freestream Measurement	23
4.2 Mean Velocity	24
4.2.1 NACA 0020 Symmetric Aerofoil	24
4.2.2 NACA 4420 Cambered Aerofoil	24
4.3 Instantaneous Velocity	27
4.3.1 NACA 0020 Symmetric Aerofoil	27
4.3.2 NACA 4420 Cambered Aerofoil	27
4.4 Turbulence Kinetic Energy	30
4.4.1 NACA 0020 Symmetric Aerofoil	30
4.4.2 NACA 4420 Cambered Aerofoil	30
4.5 Errors	33
5 Discussion	33
5.1 Lift and Drag	33
5.2 Turbulence and Coherent Structures	35
6 Conclusion	35

References	39
A Aerofoil Models	40
A.1 Styrofoam Cut Engineering Drawings	40
A.2 Manufacturing Process	41
B MATLAB Code	41
B.1 Freestream Data Processing	41
B.2 Aerofoil Flow Field Data Processing	42
B.3 Figure Creation	43

Acknowledgements

To Dr. Christina Vanderwel, my supervisor at the University of Southampton, without whom I would've never had the opportunity to conduct the particle image velocimetry experiments. Whose guidance and patience allowed me to craft and conduct such a meaningful experiment.

To my mentor, Dr. Andrew Hamilton, whose support, guidance, and frankness were instrumental to my success at Quest University.

To the staff and faculty at the University of Southampton, who helped me in the design of my experiment and taught me a sizeable portion of my knowledge in fluid dynamics.

To the staff and faculty at Quest University, who have taught and shaped me into the person I am and helped me all along my way through my degree at Quest University.

Finally, to my friends and family, whose unwavering support is the only reason I am where I am today.

Abstract

This report investigates the different lift and drag properties of symmetric and cambered aerofoils at different angles of attack. NACA 0020 symmetric aerofoils and NACA 4420 cambered aerofoils were placed at angles of attack $\alpha = -10^\circ$ to $\alpha = 20^\circ$ at 5° increments in low Reynolds number flow ($Re_c \approx 2 \times 10^4$) using a low speed water tunnel. Particle image velocimetry (PIV) was used to determine an instantaneous velocity field around each aerofoil at the differing angles of attack. The data were used to calculate an average velocity field and a turbulence kinetic energy field. The generated flow fields suggest that lift increases as angle of attack increases until a critical stall angle, where lift decreases and pressure drag increases. At equal, low angles of attack, the cambered aerofoil had a larger amount of lift than the symmetric aerofoil. However, at higher angles of attack, the cambered aerofoil may have less lift because of a large region of recirculatory flow. Furthermore, the data shows phenomena that suggests the turbulence created at low angles of attack are due to Kelvin-Helmhotz instabilities, and at high angles of attack are similar to blunt bodies.

Nomenclature

c	=	aerofoil chord length
D	=	drag force
\mathbf{F}	=	force
k	=	turbulence kinetic energy
L	=	lift force
m	=	mass
\mathbf{p}	=	momentum
P	=	pressure
Re_c	=	Reynolds number based on chord length, $U_\infty \cdot c/\nu$
U	=	speed
U_∞	=	freestream velocity in the x direction
\mathbf{U}	=	velocity vector with components (u, v) in 2D and (u, v, w) in 3D
U_i	=	instantaneous speed
\overline{U}	=	average speed
α	=	angle of attack (angle between freestream and aerofoil chord line)
Γ	=	circulation
μ	=	dynamic viscosity
ν	=	kinematic viscosity, μ/ρ
ρ	=	fluid density
τ	=	shear stress

1 Introduction

1.1 Motivation

Aerofoils are cross-sections of wings, which are streamlined objects that produce a force in a direction different from the direction of motion when moved through a fluid (Anderson, 2011). They are lifting bodies generally intended to provide a large force normal to the freestream (lift) with as little force in the same direction as the freestream (drag) as possible; they usually have a rounded leading edge and a sharp trailing edge (White, 2009). Whether as sails on windmills and boats, or as blades on turbines and helicopters, or as wings and stabilisers on aeroplanes, rockets and cars, there is no doubt aerofoils have been instrumental to the technological advancements in power generation, and in the transportation of people and cargo. However, with a world ever so conscious about human induced global climate change, it is imperative that aerofoils are designed to be as efficient as possible whilst having good performance, wasting as little energy as possible to achieve what is needed.

In particular, aeroplanes depend on the aerofoil for lift generation and as stabilisers. However, fuel is burned to achieve lift and overcome drag, as such, the aviation industry contributes to 2.0-2.5% of global CO₂ emissions; in fact, by 2050, the amount of carbon emitted by aviation is expected to increase from 2005 levels by 1.9-4.5 fold (ICAO, 2010). Not only that, fuel consumption is one of the most major direct operating cost to the aviation industry (Singh and Sharma, 2015). Nevertheless, we continue to rely on aviation as it connects us as a society, allowing for the transport of people and goods at a rapid pace. Aviation contributes to the growth of commerce, trade and tourism, and helps stimulate social and economic development of a country (Singh and Sharma, 2015). In order to retain those positive socio-economic impacts whilst minimising the carbon footprint of the aviation industry, one major approach is to maximise the lift to drag ratio (Lee et al., 2001). This means maximising the lift force generated by the wing and minimising drag force such that less energy is used to generate lift and overcome drag. It is therefore incredibly important to understand how aerofoils work, and how different aerofoils behave, since changing the profile of an aerofoil changes the lift and drag characteristics. To do so necessitates observing the flow field around different aerofoils at different angles of attack.

Geometrically similar aerofoils with equal chord based Reynolds number $Re_c \equiv \frac{\rho U_\infty c}{\mu}$, where U_∞ is the freestream velocity, c is the aerofoil chord length, and ρ and μ are the density and dynamic viscosity of the fluid, will approximately exhibit the same flow phenomena (White, 2009). However, it is impractical to have wind/water tunnel tests at the same high chord-based Reynolds number Re_c as modern airplanes (White, 2009). Furthermore, there are engineering applications for $Re_c < 5 \times 10^5$ flows, such as unmanned aerial vehicles and small-scale wind turbines (Yarusevych

and Boutilier, 2011). Furthermore, it was shown that at low Re_c , aerofoils of different shapes may cause flow separation which take on different characteristics depending on the angle of attack α contributing to a loss of lift, increase of drag, and vortex shedding, which plays a key role in the transition to turbulent flow (Yarusevych et al., 2009; Yarusevych and Boutilier, 2011). Despite the ubiquity of turbulence, there are few situations where we can make predictions to turbulent flow (Davidson, 2004). Moreover, previous studies of low Re_c flow around aerofoils mostly focus on symmetric aerofoils, which are symmetric across the chord line, and not cambered aerofoils, which are asymmetric across the chord line (Yarusevych et al., 2009; Huang et al., 2001). Therefore, for this project, we will analyse the flow field around symmetric and cambered aerofoils at different angles of attack in low speed water flow where $Re_c \approx 2.0 \times 10^4$.

1.2 Objectives

The two different types of aerofoils we will be analysing are symmetric and cambered aerofoils. We will use those aerofoils to create two-dimensional flow fields and turbulence kinetic energy fields in low Reynolds number flow at different angles of attack. In doing so, we hope to achieve the following:

1. Determine differences in lift and drag for:
 - (a) symmetric and cambered aerofoils, and
 - (b) different angles of attack.
2. Observe turbulent flow and coherent structures created by aerofoils at low Reynolds number flow.

2 Analytical Background and Literature Review

2.1 Basic Fluid Dynamics Principles

A fluid is defined as “a substance that deforms continuously under an applied shear stress or, equivalently, one that does not have a preferred shape,” including liquids and gasses (Kundu et al., 2012). Unlike solids, it is currently impossible to predict exactly how fluids will act as each particle can move on its own, meaning nearly all macroscopic flows are turbulent (Kundu et al., 2012). Turbulent flows involve fluctuations whose details are yet to be predicted by deterministic analysis nor by statistical analysis (Kundu et al., 2012). Nonetheless, we have made observations that have advanced our ability to predict the behaviours of fluids. One of the first inklings we had in the analysis fluid mechanics came from Isaac Newton in 1687: he found that some common fluids (now known as *Newtonian fluids*), including water,

air, and oil, in one-dimensional flow followed the law

$$\tau = \mu \frac{du}{dy}, \quad (2.1)$$

where τ is the shear stress on the fluid; μ is the dynamic viscosity of the fluid, a property of the fluid measured in kg/(m·s); and $\frac{du}{dy}$ is the velocity gradient with respect to the axis perpendicular to direction of the shear stress (White, 2009). Furthermore, Newtonian fluids follow the *no-slip condition*, meaning that particles adjacent to the wall move with the wall at its velocity (Tanner and Walters, 1998).

The next innovation in fluid mechanics was written first by Daniel Bernoulli in 1738: he used the principle of conservation of energy and found that for a steady frictionless incompressible flow along a streamline, where subscripts 1 and 2 represent points along the streamline,

$$\frac{P_1}{\rho} + \frac{1}{2}U_1^2 + gz_1 = \frac{P_2}{\rho} + \frac{1}{2}U_2^2 + gz_2 = \text{const.}, \quad (2.2)$$

where P , ρ and U are the fluid's static pressure, density, and velocity respectively; g is acceleration due to gravity; and z is the elevation above some reference point, where the positive direction is opposite the direction of g (White, 2009). The equation cannot account for energy exchange due to heat or external work. Nonetheless, this can be used on liquids and gasses, as liquids are nearly incompressible and gasses travelling below 0.3 times the speed of sound (commonly known as Mach or Ma 0.3) behave like incompressible fluids (White, 2009). With this equation, we can assume that in many incompressible-flow Bernoulli analyses that elevation changes are negligible, then Equation (2.2) reduces to

$$P_1 + \frac{1}{2}\rho U_1^2 = P_2 + \frac{1}{2}\rho U_2^2 = P_0 = \text{const.}, \quad (2.3)$$

where P_0 is the stagnation pressure, or the fluid pressure when its velocity is zero (White, 2009). This means that a particle along a streamline travelling at a higher velocity has a lower pressure than one travelling slower on the same streamline. Furthermore, although different streamlines may have different constants, this is rare, as irrotational flow regions (where $\nabla \times \mathbf{U} = 0$), which include all frictionless flows, will have the same constant (White, 2009). This principle, combined with the conservation of flow rate, which for incompressible flow can be written as

$$A_1 U_1 = A_2 U_2, \quad (2.4)$$

where A is the area in which the fluid flows through and the subscripts represent two points of a flow, is a powerful tool for the analysis of control volumes (White, 2009).

Leonard Euler was the first person to give a complete mathematical derivation of Equation (2.2) in 1755 and in 1757 published what later became known as the Euler equations, which were applicable to frictionless irrotational flow (White, 2009; Euler, 1757). This was generalised to what is now known as the Navier-Stokes equation in the 19th century by Claude-Louis Navier and Sir George Stokes (White, 2009). The following derivation of the Navier-Stokes equation comes from White (2009) and starts by considering an infinitesimal three-dimensional elemental box of size (dx, dy, dz) . We then impose that mass is conserved. Each side of the element is approximately one-dimensional and the change in mass m over time t for a one-dimensional system is given by,

$$\frac{dm}{dt} = \int_{CV} \frac{\partial \rho}{\partial t} dV + \sum_k (\rho_k A_k U_k)_{\text{out}} - \sum_k (\rho_k A_k U_k)_{\text{in}}, \quad (2.5)$$

where the first term describes the change in mass within the control volume over time, the second and third term describes the mass flow on the outlet and inlet control surfaces; and where dV denotes the infinitesimal volume in the system, and A denotes the area of the elemental surface. For an infinitesimal element the volume integral of the first term reduces to

$$\int_{CV} \frac{\partial \rho}{\partial t} dV \approx \frac{\partial \rho}{\partial t} dV.$$

For each face we can write the outlet mass flow and the inlet mass flow, for example, the x face has an outlet mass flow of $[\rho u + \frac{\partial}{\partial x}(\rho u) dx] dy dz$, and an inlet mass flow of $\rho u dy dz$ the difference of which is

$$\left[\rho u + \frac{\partial}{\partial x}(\rho u) dx \right] dy dz - \rho u dy dz = \frac{\partial}{\partial x}(\rho u) dx dy dz = \frac{\partial}{\partial x}(\rho u) dV.$$

Similarly for faces y and z , the difference in the outlet and inlet mass flows are given by $\frac{\partial}{\partial y}(\rho v) dV$ and $\frac{\partial}{\partial z}(\rho w) dV$ respectively. Applying conservation of mass we have $\frac{dm}{dt} = 0$, therefore introducing the above into Equation (2.5), we get,

$$\frac{\partial \rho}{\partial t} dV + \frac{\partial}{\partial x}(\rho u) dV + \frac{\partial}{\partial y}(\rho v) dV + \frac{\partial}{\partial z}(\rho w) dV = 0,$$

where we cancel out the elemental volume to obtain the continuity equation:

$$\frac{\partial \rho}{\partial t} + \frac{\partial}{\partial x}(\rho u) + \frac{\partial}{\partial y}(\rho v) + \frac{\partial}{\partial z}(\rho w) = 0,$$

which can be more concisely written as

$$\frac{\partial \rho}{\partial t} + \nabla \cdot (\rho \mathbf{U}) = 0, \quad (2.6)$$

where ∇ represents the differential operator. For incompressible flows, where ρ is constant over space and time, this simplifies to

$$\nabla \cdot \mathbf{U} = 0. \quad (2.7)$$

Now that we have built the continuity equation, we must consider the same element with respect to momentum $\mathbf{p} \equiv m\mathbf{U}$. We begin with Newton's second law of motion which states that the net force \mathbf{F} on an object is a change in momentum, therefore

$$\sum \mathbf{F} = \frac{d\mathbf{p}}{dt} = \frac{d}{dt} (m\mathbf{U}),$$

which by the chain rule gives us,

$$\sum \mathbf{F} = \mathbf{U} \frac{dm}{dt} + m \frac{d\mathbf{U}}{dt}. \quad (2.8)$$

In the continuity equation for the elemental volume, we let $\frac{dm}{dt} = 0$. Furthermore, the mass m in the element is equivalent to the density times the volume, i.e. $m = \rho dx dy dz$ therefore Equation (2.8) becomes

$$\sum \mathbf{F} = m \frac{d\mathbf{U}}{dt} = \rho \frac{d\mathbf{U}}{dt} dx dy dz \implies \sum \frac{d\mathbf{F}}{dV} = \rho \frac{d\mathbf{U}}{dt}, \quad (2.9)$$

where $\frac{d\mathbf{U}}{dt}$ is the total derivative and is given by $\frac{\partial \mathbf{U}}{\partial t} + (\mathbf{U} \cdot \nabla) \mathbf{U}$, which is nonlinear due to the second term. The net force is a sum of two types of forces, body forces due to external fields that act on the entire mass (gravity, magnetism, electric potential), and surface forces which are due to stresses on the sides of the control surface of our elemental volume. Generally the only body force we deal with is gravity, which is given by

$$d\mathbf{F}_{\text{grav}} = \rho \mathbf{g} dx dy dz \implies \frac{d\mathbf{F}_{\text{grav}}}{dV} = \rho \mathbf{g}. \quad (2.10)$$

The surface stresses σ_{ij} causing the surface forces are the sum of hydrostatic pressure p , which only acts towards the elemental volume on the axis normal to each control surface, plus viscous stresses τ_{ij} . The subscripts represent the surface/viscous stresses in the j direction on a face normal to the i axis. The surface stress tensor becomes

$$\sigma_{ij} = \begin{bmatrix} -p + \tau_{xx} & \tau_{yx} & \tau_{zx} \\ \tau_{xy} & -p + \tau_{yy} & \tau_{zy} \\ \tau_{xz} & \tau_{yz} & -p + \tau_{zz} \end{bmatrix}. \quad (2.11)$$

These stresses do not cause the force themselves, but rather their gradients. For example, Figure 1 shows that the leftward force $\sigma_{xx} dy dz$ is balanced out by the rightward force $\sigma_{xx} dy dz$ leaving the only net force to the right to be $\frac{\partial \sigma_{xx}}{\partial x} dx dy dz$. This is true for all six faces and yields the net surface force in the x direction as follows:

$$dF_{x,\text{surf}} = \left(\frac{\partial \sigma_{xx}}{\partial x} + \frac{\partial \sigma_{yx}}{\partial y} + \frac{\partial \sigma_{zx}}{\partial z} \right) dx dy dz. \quad (2.12)$$

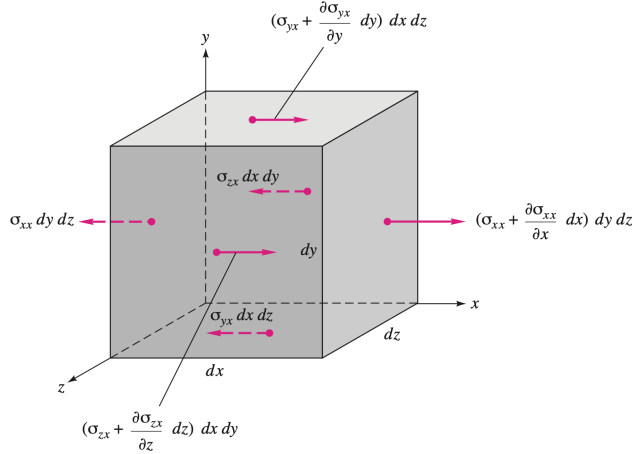


Figure 1: An elemental control volume showing all surface forces σ in the x direction on all six surfaces (White, 2009).

Using the information from the top row of the tensor from Equation (2.11), we can write Equation (2.12) as

$$\frac{dF_{x,\text{surf}}}{dV} = -\frac{\partial p}{\partial x} + \frac{\partial \tau_{xx}}{\partial x} + \frac{\partial \tau_{yx}}{\partial y} + \frac{\partial \tau_{zx}}{\partial z}. \quad (2.13)$$

Similarly, for the surface forces in the y and z directions,

$$\frac{dF_{y,\text{surf}}}{dV} = -\frac{\partial p}{\partial y} + \frac{\partial \tau_{xy}}{\partial x} + \frac{\partial \tau_{yy}}{\partial y} + \frac{\partial \tau_{zy}}{\partial z} \quad (2.14)$$

$$\frac{dF_{z,\text{surf}}}{dV} = -\frac{\partial p}{\partial z} + \frac{\partial \tau_{xz}}{\partial x} + \frac{\partial \tau_{yz}}{\partial y} + \frac{\partial \tau_{zz}}{\partial z} \quad (2.15)$$

Multiplying Equations (2.13), (2.14), and (2.15) by unit vectors \mathbf{i} , \mathbf{j} , and \mathbf{k} respectively we get

$$\begin{aligned} \left(\frac{d\mathbf{F}}{dV} \right)_{\text{surf}} &= -\nabla p + \left(\frac{d\mathbf{F}}{dV} \right)_{\text{viscous}} \\ \left(\frac{d\mathbf{F}}{dV} \right)_{\text{surf}} &= -\nabla p + \nabla \cdot \boldsymbol{\tau}_{ij}. \end{aligned} \quad (2.16)$$

The sum of Equations (2.10) and (2.16) gives us the sum of forces over the elemental volume in Equation (2.9). Therefore,

$$\rho \mathbf{g} - \nabla p + \nabla \cdot \boldsymbol{\tau}_{ij} = \rho \frac{d\mathbf{U}}{dt}, \quad (2.17)$$

which is known as Cauchy's equations of motion (Kundu et al., 2012). Equation

(2.17) can be written out in full as follows,

$$\begin{aligned}\rho g_x - \frac{\partial p}{\partial x} + \frac{\partial \tau_{xx}}{\partial x} + \frac{\partial \tau_{yx}}{\partial y} + \frac{\partial \tau_{zx}}{\partial z} &= \rho \frac{du}{dt} \\ \rho g_y - \frac{\partial p}{\partial y} + \frac{\partial \tau_{xy}}{\partial x} + \frac{\partial \tau_{yy}}{\partial y} + \frac{\partial \tau_{zy}}{\partial z} &= \rho \frac{dv}{dt} \\ \rho g_z - \frac{\partial p}{\partial z} + \frac{\partial \tau_{xz}}{\partial x} + \frac{\partial \tau_{yz}}{\partial y} + \frac{\partial \tau_{zz}}{\partial z} &= \rho \frac{dw}{dt}.\end{aligned}\quad (2.18)$$

For frictionless flow, $\tau_{ij} = 0$, which gives rise to Euler's equations:

$$\rho \mathbf{g} - \nabla p = \rho \frac{d\mathbf{U}}{dt}. \quad (2.19)$$

However, for viscous flows with Newtonian fluids, we must apply Equation (2.1) in three-dimensions which can be found changes to

$$\tau_{ij} = \mu \left(\frac{\partial u_i}{\partial x_j} + \frac{\partial u_j}{\partial x_i} \right), \quad (2.20)$$

where u_i is the fluid speed in the i direction and x_j is the j spatial coordinate. Using Equation (2.20), Equation (2.18) becomes

$$\begin{aligned}\rho g_x - \frac{\partial p}{\partial x} + \mu \left(\frac{\partial^2 u}{\partial x^2} + \frac{\partial^2 u}{\partial y^2} + \frac{\partial^2 u}{\partial z^2} \right) &= \rho \frac{du}{dt} \\ \rho g_y - \frac{\partial p}{\partial y} + \mu \left(\frac{\partial^2 v}{\partial x^2} + \frac{\partial^2 v}{\partial y^2} + \frac{\partial^2 v}{\partial z^2} \right) &= \rho \frac{dv}{dt} \\ \rho g_z - \frac{\partial p}{\partial z} + \mu \left(\frac{\partial^2 w}{\partial x^2} + \frac{\partial^2 w}{\partial y^2} + \frac{\partial^2 w}{\partial z^2} \right) &= \rho \frac{dw}{dt},\end{aligned}\quad (2.21)$$

which can be rewritten as

$$\rho \mathbf{g} - \nabla p + \mu \nabla^2 \mathbf{U} = \rho \frac{d\mathbf{U}}{dt}, \quad (2.22)$$

where ∇^2 is the Laplacian operator. In conjunction with the incompressible continuity equation (Equation (2.7)), the four equations constitute what is known as the incompressible Navier-Stokes equations.

The momentum equations of the Navier-Stokes equations can be manipulated such that all terms are non-dimensionalised (White, 2009). By doing so, Osborne Reynolds in 1883 brought about the primary parameter defining the properties of a fluid, now known as the Reynolds number, a dimensionless parameter:

$$Re \equiv \frac{\rho U l}{\mu} = \frac{U l}{\nu} \quad (2.23)$$

where U and l are the velocity and length scales respectively and ν is the kinematic viscosity, defined as a ratio of dynamic viscosity μ to density ρ (White, 2009). It indicates whether or not the flow is creeping, laminar, or turbulent flow when the Reynolds number is very low, moderate, or high respectively; it measures the ratio between inertial and viscous forces (White, 2009; Anderson, 2011). For incompressible immersed flow, as long as geometry and Reynolds number is preserved, then the flow field will behave the same (White, 2009). When applied to aerofoils, we use a chord-based Reynolds number Re_c , where we use the freestream velocity of the fluid U_∞ as the velocity scale and the aerofoil's chord length c as the length scale (White, 2009).

Despite a full description of the behaviour of incompressible fluids via the Navier-Stokes equations, due to the fact that they are a coupled system of nonlinear partial differential equations, there does not exist a general closed form analytical solution (Anderson, 1995). There are therefore two avenues that we turn towards for predicting fluid flows, the first being the relatively new computational fluid dynamics (CFD) which employs numerical solutions of the Navier-Stokes equations (usually with significant approximations); the other being physical experimentation which not only allows us to see actual flows but allows us to confirm the validity of CFD models (Anderson, 1995).

2.2 Aerofoils

Unless otherwise stated, the information in this section is from Anderson (2011).

An aerofoil has a leading and trailing edge, which are the front and rear points of an aerofoil and are usually in the shape of a teardrop, round at the leading edge, sharp at the trailing edge; it has a mean camber line which is a line that traces the middle point between the upper and lower surfaces; the chord c of an aerofoil is the length of the chord line, a straight line between the leading and trailing edge; the camber is the maximal distance between the mean camber line and the chord line; the thickness is the maximal distance (perpendicular to the chord line) between the upper and lower surfaces; and its angle of attack α is the angle between the freestream velocity and the chord line.

To create a standardised set of aerofoils, the National Advisory Committee for Aeronautics (NACA), which has since been absorbed by the National Aeronautics and Space Administration (NASA), created several families of aerofoils with analytic descriptions of the aerofoil and camber lines in the 1930s, one of which is the NACA 4-series aerofoils (Anderson, 2016; Ladson, 1975). A NACA 4-series aerofoil is given by 4 digits, the first digit gives the maximum camber as a percentage of the chord; the second digit gives the position of the camber in tenths of the chord; and the last two digits represent the maximum thickness as a percentage of the chord (Jacobs et al., 1933). Jacobs et al. (1933) writes that the thickness y_t for a 4-series aerofoil

is approximately given by,

$$\pm y_t = 5t(0.29690\sqrt{x} - 0.12600x - 0.35160x^2 + 0.28430x^3 - 0.10150x^4) \quad (2.24)$$

where x is the position along the aerofoil as a fraction of the chord and t is the maximum thickness as a fraction of the chord (i.e. the last two digits divided by 100). Equation (2.24) gives the aerofoil shape for a 4-series aerofoil with no camber, i.e. a symmetric NACA 00xx aerofoil. For a cambered aerofoil, with asymmetric upper and lower surfaces, we must consider the mean camber line which is given by,

$$y_c = \begin{cases} \frac{a}{b^2} [2bx - x^2] & 0 \leq x < b \\ \frac{a}{(1-b)^2} [(1-2b) + 2bx - x^2] & b < x \leq 1, \end{cases} \quad (2.25)$$

where a is the maximum camber as a fraction of the chord, i.e. the first digit divided by 100; and b is the location of maximum camber as a fraction of the chord, i.e. the second digit divided by 10 (Jacobs et al., 1933). Since the thickness must be applied perpendicular to the mean camber line, then the upper and lower parts of the aerofoil are given by

$$y_u = y_c + y_t \cos \theta \quad \text{and} \quad y_l = y_c + y_t \cos \theta \quad (2.26)$$

respectively, where $\theta = \arctan \frac{dy_c}{dx}$ (Jacobs et al., 1933). Evaluating the derivative we find that,

$$\frac{dy_c}{dx} = \begin{cases} \frac{2a}{b^2} (b-x) & 0 \leq x < b \\ \frac{2a}{(1-b)^2} (b-x) & b < x \leq 1. \end{cases} \quad (2.27)$$

Equations (2.24) & (2.26) when drawn out on a Cartesian plane will give the profile of a 4-series symmetric and cambered aerofoils respectively, where $(0, 0)$ is the leading edge and $(1, 0)$ is the trailing edge.

2.2.1 Lift

A streamline with some curvature has some centripetal force that must be created by a pressure gradient across the streamline increasing in the direction opposite to the centre of the curvature (Babinsky, 2003). An aerofoil at certain angles of attack will bend the flow such that the curvatures of streamlines above and below the aerofoil faces down. By curving the streamlines and giving the fluid a downward velocity component, the reaction force of the deflected fluid (from Newton's third law) will act on the aerofoil upwards (Resnick et al., 1988). This upward force is caused by a pressure difference between the upper and bottom surfaces of an aerofoil. If we take a simple "aerofoil", a curved plate producing lift, as shown in Figure 2, we see the curved streamlines above and below the aerofoil. Above the aerofoil, the streamline's curvature gradually straightens as we travel from point B to point A on Figure 2 until it becomes completely straight, undisturbed by the

aerofoil; since the curvature faces downwards, this means that there is an increasing pressure gradient until we reach atmospheric pressure (Babinsky, 2003). Similarly, below the aerofoil, the curvatures also face downwards, meaning as we move from point D to point C on Figure 2, there is a decreasing pressure gradient tending towards atmospheric pressure (Babinsky, 2003). Since the pressure at point B above the aerofoil is below atmospheric pressure and the pressure at point D below the aerofoil is above atmospheric pressure, then it must be true that the pressure below the aerofoil is greater than the pressure above, causing an upwards force called lift. Lift increases as angle of attack α increases until it reaches a critical stall angle where lift begins to fall. A symmetric aerofoil has no lift at $\alpha = 0^\circ$, whereas a cambered aerofoil has some finite lift at $\alpha = 0^\circ$.

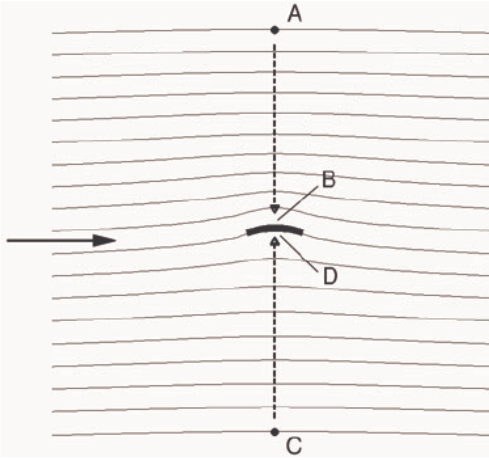


Figure 2: Streamlines around a lifting curved plate travelling through a fluid; A and C are points far above and below the plate, and B and D are points directly above and below the plate (Babinsky, 2003).

To calculate lift we can use a concept called circulation. An aerofoil producing lift will have a velocity field around the aerofoil such that the line integral of the velocity along a curve A enclosing the aerofoil, defined as circulation Γ , will be finite, where

$$\Gamma \equiv \oint_A \mathbf{V} \cdot d\mathbf{s}. \quad (2.28)$$

Using circulation, the Kutta-Joukowsky theorem finds that we can calculate the lift per unit span L' of an aerofoil as follows

$$L' = \rho_\infty U_\infty \Gamma, \quad (2.29)$$

where ρ_∞ and U_∞ are the density and speed of the fluid at a point far upstream of the aerofoil; this relation can be found through the use of complex variables and

flow potentials in inviscid flow. This relation allows us to calculate lift through circulation. Furthermore, circulation shows an increase in speed above the aerofoil and a decrease in speed below the aerofoil. This is consistent with Bernoulli's principle from Equation (2.3), as the difference in speed means that the pressure above the aerofoil is lower than the pressure below the aerofoil.

The generation of circulation on an aerofoil is due to a starting vortex. Consider an aerofoil at rest, then the circulation of the fluid particles in an arbitrary curve around it is zero. You then move the aerofoil through a fluid to the left, then the flow below the aerofoil will start to curl around the trailing edge at high velocity, meeting the flow above and forming a stagnation point, where the flow velocity is zero and pressure is highest. This creates a region of high vorticity, and as it moves downstream, it rolls up and forms a vortex known as the starting vortex. The flow cannot sustain moving around the sharp corner at the trailing edge of an aerofoil, the stagnation point moves backwards until it reaches the trailing edge (known as the Kutta condition) and the flow separates reaching a steady state (White, 2009). The starting vortex, having moved downstream, has some circulation anti-clockwise; however the total circulation around the vortex and the aerofoil cannot change from the original value at rest, therefore clockwise circulation must occur around the aerofoil.

2.2.2 Drag

There are three main types of drag on a wing in subsonic flow, induced drag, skin-friction drag, and pressure (or form) drag: the former occurs only when we consider a finite wing in three-dimensions; the latter two, however, must be considered for aerofoil sections in infinite span wings. Skin-friction drag comes from the shear stresses acting on the surface from viscosity. Although the formulation of lift in terms of circulation uses inviscid flow, surface friction is essential in creating a very thin layer dominated by viscous forces from the surface, known as a boundary layer, that remains attached to the aerofoil to bend the streamline and achieve the Kutta condition. Over an aerofoil, the boundary layer usually starts out with low skin-friction drag laminar flow and transitions to a higher drag turbulent boundary layer downstream of the leading edge. However, this boundary layer can sometimes separate from the body, which causes pressure drag and a loss of lift known as stall.

As the fluid flows past the top surface of an aerofoil, there is a smooth velocity profile with no inflections on the boundary layer from $U = 0$ at the surface (no-slip condition) to approximately freestream velocity. However, as the fluid moves further down the aerofoil, the aerofoil falls away (especially at higher angles of attack), and the fluid must expand to fill the space. As it expands, Equation (2.4) means that the fluid speed must slow and, by Bernoulli's principle (Equation (2.3)), must increase in pressure as the fluid moves along in the flow direction. This creates what is known

as an adverse pressure gradient where $\frac{dP}{dx} > 0$. The greater the angle of attack, the more the fluid expands, the stronger the adverse pressure gradient. A fluid moving against an adverse pressure gradient will begin to slow until it is eventually stationary (where the inflection point of the velocity profile is at the surface) or even reversing and moving backwards (where the inflection point of the velocity profile is above the surface). When backflow occurs, the flow will separate from the surface, creating a region of recirculation at the rear of the aerofoil.

Subsonic inviscid two-dimensional flow that is attached to the surface will have pressure in the the rearwards direction (near the leading edge) counteracted equally by pressure in the forward direction (near the trailing edge); however, separated flow will cause a loss of pressure in the separated region, therefore the rearwards pressure in the front will overcome the forward pressure in the rear causing pressure drag. Furthermore, and perhaps more importantly, as the angle of attack increases, the boundary layer separation moves forwards along the aerofoil until the flow is completely separate from the upper surface, and the lift force decreases markedly as the streamline directly above the aerofoil is no longer curved downwards, this is known as stall (White, 2009). Flow separation can be delayed along the aerofoil with a turbulent boundary layer (possibly created by vortex generators) by moving in more energetic, faster flow towards the aerofoil surface; this is why golf balls with dimples travel much further than those without (White, 2009; Kundu et al., 2012).

2.3 Low Reynolds Number Flow

As mentioned in Section 1.1, aerofoils in low chord-based Reynolds number flow at $Re_c < 500 \times 10^3$ is susceptible to a shear boundary layer separation (Yarusevych et al., 2009). This separated boundary layer does not reattach leading to coherent structures formed in the shear layer which may be due to Kelvin-Helmholtz instabilities, which are caused by two fluid interfaces travelling at different velocities and creates a cat's eye pattern (Yarusevych et al., 2009; Watmuff, 1999; Friedlander and Lipton-Lifschitz, 2003). It may also form coherent structures during the transition of the shear layer from laminar to turbulent flow (Hsiao et al., 1989).

Furthermore, coherent structures, whose characteristics depend of the behaviour of the separated shear layer, can form in the wake of an aerofoil at low Reynolds numbers (Yarusevych and Boutilier, 2011). “At high poststall angles of attack, the wake of an [aerofoil] is similar to that of a bluff body” as opposed to a streamlined body (Yarusevych and Boutilier, 2011). Whereas at lower angles of attack, it has been shown that the wake differs from that of a bluff body (Yarusevych et al., 2009; Huang et al., 2001).

3 Methodology

3.1 Particle Image Velocimetry (PIV)

In this experiment, we experimentally determined the flow field around the two NACA 0020 and NACA 4420 aerofoils in low Reynolds number flow at different angles of attack. With the advent of high resolution digital cameras and increased computing power, particle image velocimetry (PIV) has become the primary method to study fluid flows in experimental fluid mechanics over the past few decades, as it can provide spatial derivatives, flow visualisations, and has a capability for spatial correlation, unlike other methods such as hot-wire anemometry (HWA) and laser-Doppler velocimetry (LDV) (Westerweel et al., 2013). Furthermore, unlike indirect methods like HWA and pressure probes, PIV allows for instantaneous measurements of the whole velocity field and does not disturb the flow or flow properties, except for the tracer particles which are chosen to have negligible effect to the flow (Raffel et al., 2018). We will therefore employ PIV for this experiment.

The most basic PIV is a basic planar system consisting of a double pulsed laser forming a single light-sheet through optics shining on seeded particles in the fluid; a single lens digital camera then captures multiple frames of the scattered light from the particles dispersed in a wind/water tunnel in quick succession (Adrian and Westerweel, 2011). The captured images are then divided into small interrogation regions and the mean displacement of each region is found by cross-correlating between two frames (Westerweel et al., 2013). Its maximum correlation can be found with sub-pixel accuracy by fitting a Gaussian (or similar function) to the highest correlation peak (Westerweel et al., 2013). The displacements, divided by the known time delay between the two frames are used to find the instantaneous velocity of the fluid flow field.

3.2 Water Tunnel

To facilitate PIV, all physical experimentation was conducted in the Rolling Hills Research Corporation Model 0710 University Desktop recirculating water tunnel at the University of Southampton (Figure 3). A wind tunnel would allow for higher freestream velocity. Nonetheless, a water tunnel was chosen as it allows us to use bigger seeding particles that is neutrally buoyant and can be easily mixed into the fluid for PIV, thereby decreasing complexity, reducing the need for a high-powered laser, and reducing costs (Raffel et al., 2018).

3.3 Aerofoil Model

Based on the facilities of the University of Southampton, it was decided that the best and most cost effective way of creating the aerofoils was to cut them from blocks of Styrofoam and to cover it with Solarfilm - a self-adhesive iron-on covering

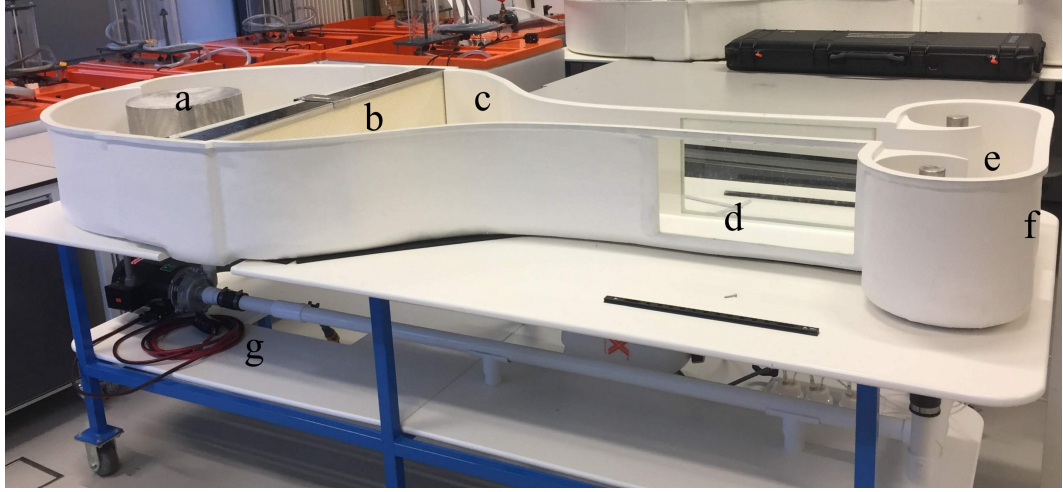


Figure 3: Rolling Hills Research Corporation Model 0710 recirculating water tunnel with a) the settling chamber, b) flow conditioning elements, c) the flow contraction section, d) the test section, e) the flow exit section, f) a glass panel (not in view), and g) the flow return line and pump.

usually used for remote control planes - to ensure a smooth surface (Solarfilm Sales Ltd, 2020). To achieve our objectives, the aerofoils chosen were two NACA 4-series aerofoils of equal thickness, the NACA 0020 symmetric aerofoil and the NACA 4420 cambered aerofoil. The 20% thickness allowed for easy manufacturing without being too thick, and the camber was chosen to allow for significant differences in the flow. To cut them from Styrofoam we used Equations (2.24) & (2.26) to construct an aerofoil as a CAD file in Solidworks with span length equal to chord length at 1cm. The model was then scaled to the dimensions of the mounting rack for the water tunnel (164mm). The formulae used to create the aerofoil does not actually close at $\frac{z}{c} = 1$, however, since the hot wire Styrofoam cutter is unable to turn sharp edges close to 360° , a circle of radius 5mm connecting the two loose ends was added. Furthermore, a 1.5mm radius hole was made on the chord line 39mm from the leading edge of the aerofoil to insert a rod for the mounting rack, the cut was made using an inverted ‘L’ inset 1mm wide. Engineering drawings for the Styrofoam cut can be found in Appendix A.1.

A block of styrofoam was first cut to be 164mm deep. Then two of each of the aerofoil shapes were cut out (Appendix A.2a). For each aerofoil, the cylinder created by the extra round shape at the end was sliced off with a knife. An aluminium rod with a 3mm diameter and 174mm long was filed down with sandpaper to prevent scraping the glass test section window, put through the hole such that it jutted out by 5.5mm on the right side and 10mm on the left and glued down with Adralite® Standard epoxy (Appendix A.2b). This extrusion is used for the main mount. A

heated stick of approximately 3mm diameter was pushed into the left side of the aerofoil 43mm behind the machine cut hole on the chord of the aerofoil 2-3cm deep. Another 3mm diameter aluminium rod, jutting out 10mm, was glued into the hole using epoxy (Appendix A.2b), this is used for the adjustable mount used to adjust angle of attack and can be used with the main mount to measure angle of attack. Finally, a layer of Solarfilm was applied using an iron to ensure the surface is as smooth as possible (Appendix A.2c & A.2d).

3.4 Setup and Data Collection

Room temperature tap water ($\sim 20^{\circ}\text{C}$) was used to fill the water tunnel until the water level was approximately the height of the element in the settling chamber (Figure 3a). Due to equipment restrictions, instead of a pulsed laser, which would minimise the appearance of streaks captured in each image, we used a class 3R continuous collimated laser diode with 532nm wavelength light at 4.5mW (Thorlabs, 2011). A set of cylindrical and spherical lenses with focal length $f = -9.7\text{mm}$ and $f = 300\text{mm}$ respectively were used to dispersed into a plane of light, lowering the system to a class 2 laser. This was then mounted onto the table of the water tunnel behind the glass panel (Figure 3f) such that it shone through the centre of the test section parallel to the test section windows (Figure 3d). VESTOSINT[®] 2157 particles, which are approximately $56\mu\text{m}$ in diameter (Evonik, 2015), was added to the water such that approximately 5-15 particles would illuminate per cm^2 on the laser sheet created by the mounted laser. The aerofoil was then mounted into the test section to make measurements. The test section window was found to be 237mm tall and 455mm wide, the water level was very slightly higher than the glass and the mounting point was 121mm from the top of the glass and 157mm from the front of the test section window. Furthermore, the test section width at the mount is 180mm and increases to 190mm at the rear of the test section window. To choose the focal length f of the lens on our camera, the JAI GO-2400-USB 2.35-megapixel camera (JAI, 2020), we use the formula:

$$f = \frac{M \cdot l}{(M + 1)^2}, \quad (3.1)$$

where l is the focal distance (i.e. the distance from the object plane to the sensor image plane), and M is the magnification (i.e. the ratio between the sensor image size and the size of the object plane).

We therefore measured the desired analysis section to be approximately 350mm wide and found the camera to have a sensor with a width of 11.3mm (JAI, 2020). Therefore, $M = \frac{11.3\text{mm}}{350\text{mm}}$. The camera was mounted on the rail next to the test section window and the distance from the laser sheet to the sensor, equivalent to focal distance l , was found to be approximately 415mm. Thus, using Equation (3.1),

we find the focal length to be

$$f = \frac{\frac{11.3\text{mm}}{350\text{mm}} \cdot 415\text{mm}}{\left(\frac{11.3\text{mm}}{350\text{mm}} + 1\right)^2} \approx 12.57\text{mm}. \quad (3.2)$$

The lens with the closest focal length is the 12mm lens. That lens was therefore mounted on the JAI camera, which was connected to a computer with JAI software. Furthermore, lights were turned off and black paper was used to surround the test section with the camera to block out as much external light as possible. Test runs with the aerofoil with the water velocity at maximum were used to pick the frame rate based on a balance between exposure time and possible light streaks (from high exposure time and high velocity). An optimum frame rate was found to be 119.933Hz, for which the maximum exposure time is 8270 μ s. Furthermore, each capture set was configured to be 240 frames (i.e. approximately 2s of capture time) in jpeg format.

Firstly, the aerofoil was taken out and a ruler was put in the laser plane and captured by the camera for a reference length with the water at zero velocity. Then, the pump for the water tunnel was set to maximum and one capture of 2 seconds were recorded for the freestream velocity measurement. Then, a NACA 0020 aerofoil was mounted in the water tunnel at $\alpha = -10^\circ$ as measured with a protractor and allowed to settle for ~ 30 s. A 240 frame capture was recorded, saved, and a second trial was conducted. The same 2×240 frames were captured for angles of attack $\alpha = -5^\circ, 0^\circ, 5^\circ, 10^\circ, 15^\circ$, and 20° . This process was repeated for a NACA 4420 aerofoil, then for the other NACA 0020 and NACA 4420 aerofoil. Figure 4 shows the setup for the experiment.

3.5 Data Analysis

The jpeg data were analysed using the open source MATLAB application PIVLab (Thielicke, 2019). Firstly, a calibration image of the ruler in the laser plane was loaded and it was found that 50mm corresponded to 289.22px and the time step between each frame was given as $\frac{1}{119.933\text{Hz}} \approx 8.338\text{ms}$. The images of each capture were loaded, the region of interest selected, and masks drawn such that the aerofoil, the parts of the plane in the image picture not illuminated/not strongly illuminated by the laser, and the visible edge of the aerofoil mount were excluded from the PIV analysis. The image was then pre-processed by the software with CLAHE (window size 20px), highpass (kernal size 20px), Wiener2 denoise filter (window size 3px), and auto contrast stretch enabled. These were chosen based on which gave the best contrast in the preview. Then, we used FFT window deformation PIV analysis between every two frames with three passes of 128px, then 64px, then 32px. We chose this by trial and error, where we attempted to minimise final pass size for denser vectors at the cost of errors due to lack of correlated pixels in the window, and this window size gave us erroneous vectors in about 10% of the image

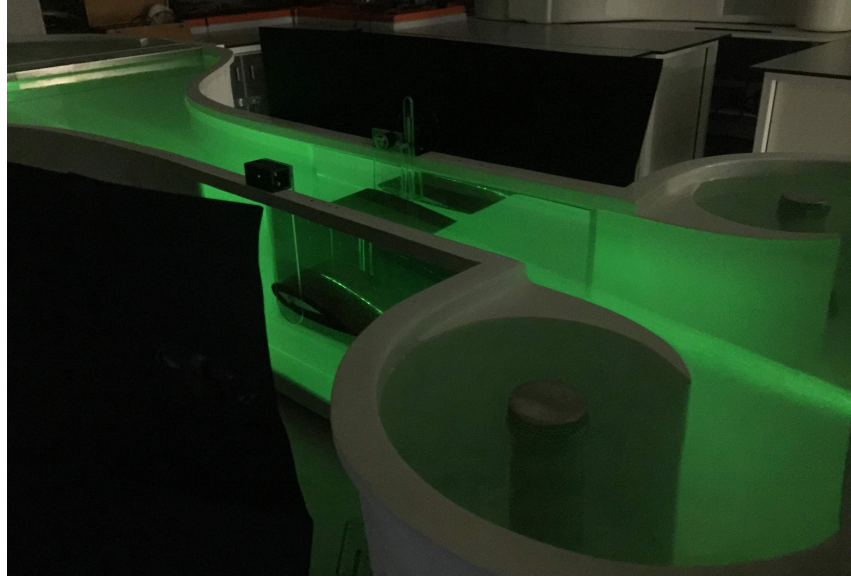


Figure 4: Experiment setup with an aerofoil mounted in the water tunnel. The laser is turned on, and the camera is mounted on a rail behind the black paper in the foreground.

area. Some of these erroneous vectors were deleted in post-processing via manual vector validation, where a scatter-plot with all the velocity data of the image set is displayed with the horizontal speed component on the x -axis and the vertical component on the y -axis and a rectangular section of the scatter-plot is selected manually to be acceptable vectors based on the density of the scatter-plot and reasonable expectations of the velocity. Other erroneous vectors were also deleted via a standard deviation filter with a $7 \times$ standard deviation threshold, and a local median filter with a threshold of 5 and ϵ set at 0.1. These deleted data were then interpolated based on surrounding velocity data by the software. The same settings were used for the freestream measurement.

The data outputted by the software was a .MATLAB workspace and included an x and y coordinate system in metres based on the calibration for each 32×32 px cell in the selected region of interest. Based on that coordinate system it had an array of the drawn mask, and cells containing 120 matrices of the u and v component of the instantaneous flow velocity between two frames for each cell. Furthermore, it was found that some random frames had the majority of velocities vectors at twice the magnitude of other frames. These sets of frames were assumed to be erroneous and marked off to be ignored in the data analysis. The freestream velocity U_∞ was found with the median value of the average speed of each cell (Appendix B.1). For each image capture, the freestream velocity was first used to non-dimensionalise the velocity components as fractions of the freestream velocity. Then, the magnitude of

the instantaneous velocities of each frame were found and stored, and the erroneous frames deleted. The mean velocity magnitudes were also found and stored. Then the turbulence kinetic energy k was calculated. k is given by half the sum of the variance of velocity components. Due to the lack of three-dimensional data we will use the two dimensional proxy for k and assume that the w velocity component is negligible. Thus,

$$k \approx \frac{1}{2} \left(\overline{(u')^2} + \overline{(v')^2} \right), \quad (3.3)$$

where the mean variance of the velocity components are given by

$$\overline{(u')^2} = \frac{1}{N} \sum_{j=1}^N (u_{i,j} - \bar{u})^2 \quad \text{and} \quad \overline{(v')^2} = \frac{1}{N} \sum_{j=1}^N (v_{i,j} - \bar{v})^2, \quad (3.4)$$

where N is the number of samples, which here is equal to the 120 correlated frames per capture. k has units m^2/s^2 which we non-dimensionalise by dividing by the square of the freestream velocity $(U_\infty)^2$. Finally, the point where $\frac{x}{c} = 1$ was used to set a reference point for the figure axes at $(1,0)$.

The figures were created using the data found above on MATLAB, including mean velocity field, a random instantaneous velocity vector field, and the turbulence kinetic energy using the code given in Appendix B.3. Due to human error, the angle of attack of each set of trials did not necessarily match up exactly to the intended angles of attack. Since for each aerofoil profile, two aerofoils were mounted at each intended angle of attack for two captures, an electronic protractor was overlaid on a picture from each angle of attack of each aerofoil to determine which of the two aerofoils with the same profile was mounted closest to the intended angle of attack. Then from these trials two sets of figures were produced from each capture and one was chosen to be shown below based on the subjective quality of data produced in the figures. This was coded in as the matrix `goodaoa` in Appendix B.3, where ‘0’ represented the trials with the angle of attack farthest from the intended, and ‘2’ represented the trial with the closer angle of attack but produced subjectively worse figures. The final figures produced were the mean flow velocities, instantaneous flow velocities (using a random number generator to pick a frame), and turbulence kinetic energy k .

4 Results

4.1 Freestream Measurement

A PIV analysis on the freestream revealed that the median value of the averaged freestream velocity field was approximately 0.12m/s. Given that the kinematic viscosity $\nu = \frac{\mu}{\rho}$ of water at approximately atmospheric pressure (1atm) and room temperature ($\sim 20^\circ\text{C}$) is $\sim 1 \times 10^{-6}\text{m}^2/\text{s}$ (International Towing Tank Conference, 2011),

and that the chord length of the aerofoil was 0.164m, the chord based Reynolds number is therefore

$$Re_c = \frac{U_\infty c}{\nu} = \frac{0.12\text{m/s} \times 0.164\text{m}}{1 \times 10^{-6}\text{m}^2/\text{s}} = 19680 \approx 2.0 \times 10^4. \quad (4.1)$$

4.2 Mean Velocity

4.2.1 NACA 0020 Symmetric Aerofoil

At all angles of attack, the average the flow above and below the NACA 0020 aerofoil were at speeds greater than U_∞ (Figure 5). Furthermore, there is a vertical region above the aerofoil at the front that has significantly slower flow than surrounding cells at all angles of attack. All angles of attack have a region of low speed flow ($< 0.5 \cdot U_\infty$) around the aerofoil. This region is approximately the same small size for $\alpha = -9^\circ, -5^\circ, 0^\circ$ and mostly below the aerofoil for the former two and above the aerofoil for the latter. For all those, there is only a small amount backflow in the streamlines of $\alpha = 0^\circ$. For $\alpha = 4^\circ$, we saw a larger area of low speed flow where there is also small amounts of backflow. For $\alpha = 10^\circ$, we saw an even larger region of low speed flow with two vortices. Finally, for $\alpha = 16^\circ, 19^\circ$, we saw a large area of low speed flow dominating the majority of the test area with a fully developed vortex.

The area outside of the area of low speed flow transitions towards speeds that range between $\sim 1 \cdot U_\infty$ and $\sim 1.5 \cdot U_\infty$. The speeds in that area increase as we go to angles of attack outside of $\alpha = 0^\circ$. Furthermore, for $\alpha < 0^\circ$ the streamlines below the aerofoil are deflected upwards; for $\alpha = 0^\circ$ the streamlines are deflected around the aerofoil and back to $\frac{y}{c} \approx 0$; for $\alpha = 5^\circ$, the streamlines above the aerofoil are deflected downwards, whereas the streamlines below are deflected down before $\frac{x}{c} \approx 0.4$ and mostly flat thereafter; and for $\alpha = 10^\circ, 16^\circ, 19^\circ$ the streamlines above are deflected downwards, whereas the streamlines below are deflected downwards before $\frac{x}{c} \approx 0.9 - 1$ and deflected upwards in the wake.

4.2.2 NACA 4420 Cambered Aerofoil

Similarly, at all angles of attack, the average the flow above and below the NACA 4420 aerofoil were at speeds greater than U_∞ (Figure 6). As well, near the top left of each speed graph is an area of lower velocity preceding the rest of the flow. Here the region of low speed flow ($< 0.5 \cdot U_\infty$) is located mostly below the aerofoil for $\alpha = -10^\circ$, mostly above the aerofoil for $\alpha = -5^\circ$, and entirely above the trailing edge for $\alpha \geq 0$. The low speed flow area is smallest for $\alpha = -5^\circ$ with no backflow, $\alpha = -10^\circ$ is slightly larger with no backflow for the former. Starting from $\alpha = 1^\circ$ The area of the low speed flow region continues to grow larger as α increases. Furthermore, each region for $\alpha \geq 0$ has a vortex, which increases in size as α increases.

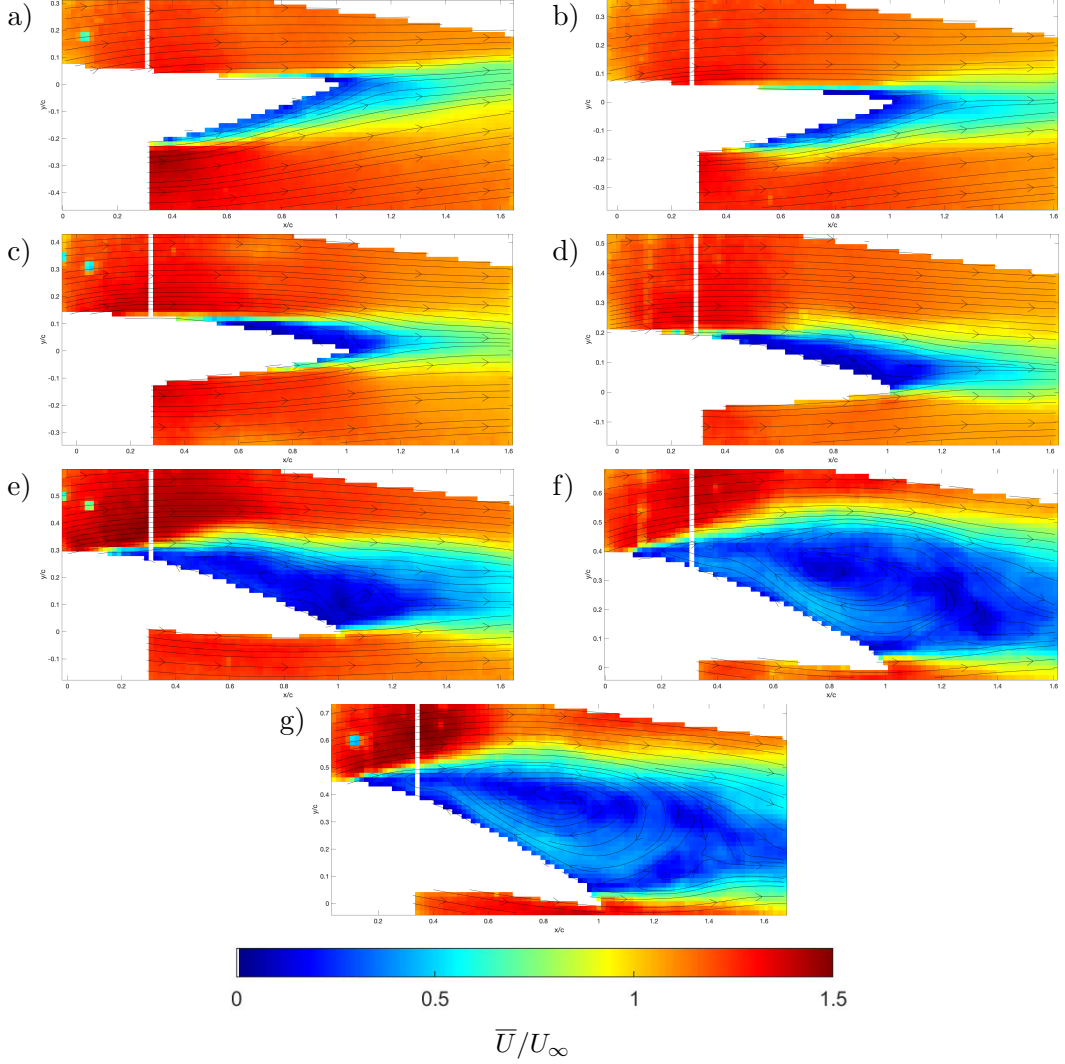


Figure 5: Mean flow velocity as a fraction of the freestream velocity and streamlines around a NACA 0020 aerofoil at $Re_c = 19.6 \times 10^3$ at (a) $\alpha = -9^\circ$ (b) $\alpha = -5^\circ$ (c) $\alpha = 0^\circ$ (d) $\alpha = 4^\circ$ (e) $\alpha = 10^\circ$ (f) $\alpha = 16^\circ$ (g) $\alpha = 19^\circ$. $(\frac{x}{c}, \frac{y}{c}) = (1, 0)$ is set at the trailing edge of the aerofoil. White sections indicate where masks were drawn over the aerofoil, the laser sheet shadow, and where not enough particles were visible.

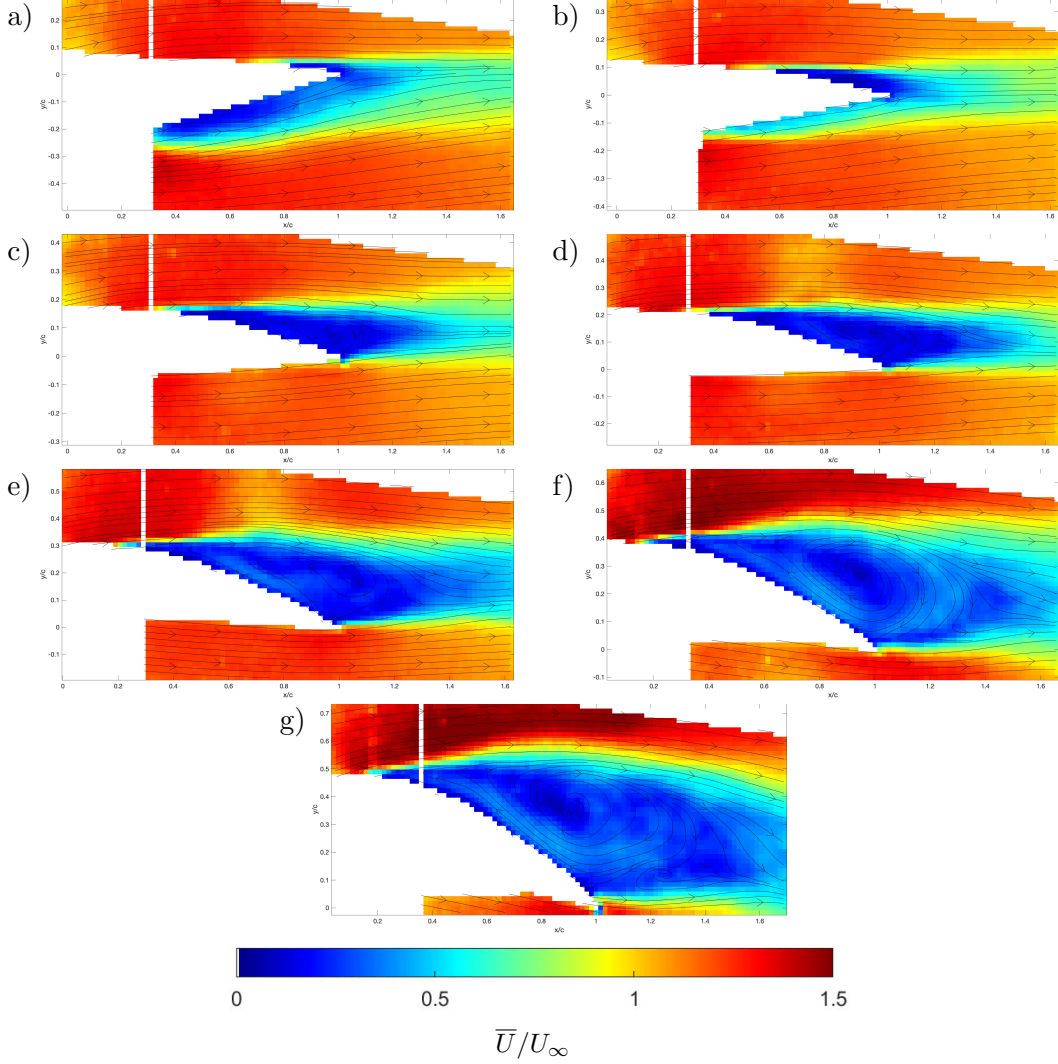


Figure 6: Mean flow velocity as a fraction of the freestream velocity and streamlines around a NACA 4420 aerofoil at $Re_c = 19.6 \times 10^3$ at (a) $\alpha = -10^\circ$ (b) $\alpha = -5^\circ$ (c) $\alpha = 1^\circ$ (d) $\alpha = 3^\circ$ (e) $\alpha = 10^\circ$ (f) $\alpha = 15^\circ$ (g) $\alpha = 20^\circ$. $(\frac{x}{c}, \frac{y}{c}) = (1, 0)$ is set at the trailing edge of the aerofoil. White sections indicate where masks were drawn over the aerofoil, the laser sheet shadow, and where not enough particles were visible.

The area outside of the region of low speed flow for the NACA 4420 aerofoil transitions towards speeds that range from $1 \cdot U_\infty$ and $1.6 \cdot U_\infty$. The speed of the flow in said region is much faster for $\alpha = 15^\circ, 20^\circ$ at $1.5 \cdot U_\infty$. It is slightly slower at about $1.3 \cdot U_\infty$ for $\alpha = 10^\circ$. It is even slower at about $1.1 \cdot U_\infty - 1.2 \cdot U_\infty$ for $\alpha = -10^\circ, -5^\circ, 1^\circ, 3^\circ$. Furthermore, for $\alpha = 3^\circ, 10^\circ$ we get regions above the aerofoil at $\frac{x}{c} \approx 0.8$ that has significantly lower speed than the surrounding flow. At $\alpha = -10^\circ$ the streamlines above the aerofoil curve downwards but the streamlines below curve upwards a lot more. At $\alpha = -5^\circ, 1^\circ, 3^\circ$, the streamlines above curve downwards whereas the streamline below likely curves downwards in the shadow region before curving slightly upwards. At $\alpha = 10^\circ, 15^\circ, 20^\circ$ the streamlines above the aerofoil are only deflected downwards at $\frac{x}{c} > 0.8$, or even past the aerofoil, whereas the streamlines below the aerofoil are deflected downwards before rising again after $\frac{x}{c} = 1$.

4.3 Instantaneous Velocity

4.3.1 NACA 0020 Symmetric Aerofoil

Here, with the instantaneous flows, the oscillations in the flow are shown more clearly (Figure 7). Each figure is a random snapshot of the time dependent flow. We saw that compared to the mean velocities in Figure 5, the low speed regions are more much more irregular. For example, structures - particularly in the wake - formed at low angles of attack (such as Figure 7a). Furthermore, these regions seemed to mix better in the wake and dissipated unlike those at higher angles of attack (such as Figure 7f). These structures with peaks and troughs are consistent with qualitative observations during the experiment.

Furthermore, as α increases from -10° , we saw the region of highest speed migrates from below the aerofoil to being approximately equal on both sides of the aerofoil for $\alpha = 0^\circ$ to being above the aerofoil. Furthermore, those regions generally increase in speed the more the angle of attack deviates from $\alpha = 0^\circ$.

4.3.2 NACA 4420 Cambered Aerofoil

As with the NACA 0020 aerofoil, with the instantaneous flows, the oscillations in the flow for the NACA 4420 aerofoil are shown more clearly as they provide a random snapshot of the time dependent flow (Figure 8). The low speed regions are again much more irregular in shape compared to the mean velocities in Figure 6. However, it seems that at $\alpha = 5^\circ$ (Figure 8d), the wake seems to only have one large coherent structure with no undulation, although this may be by chance. The wake flow is generally quite consistent with qualitative observations.

However, here the regions of highest speed looked to be approximately equal for $\alpha = -10^\circ, -5^\circ$, and those outer regions increase in speed above the aerofoil as

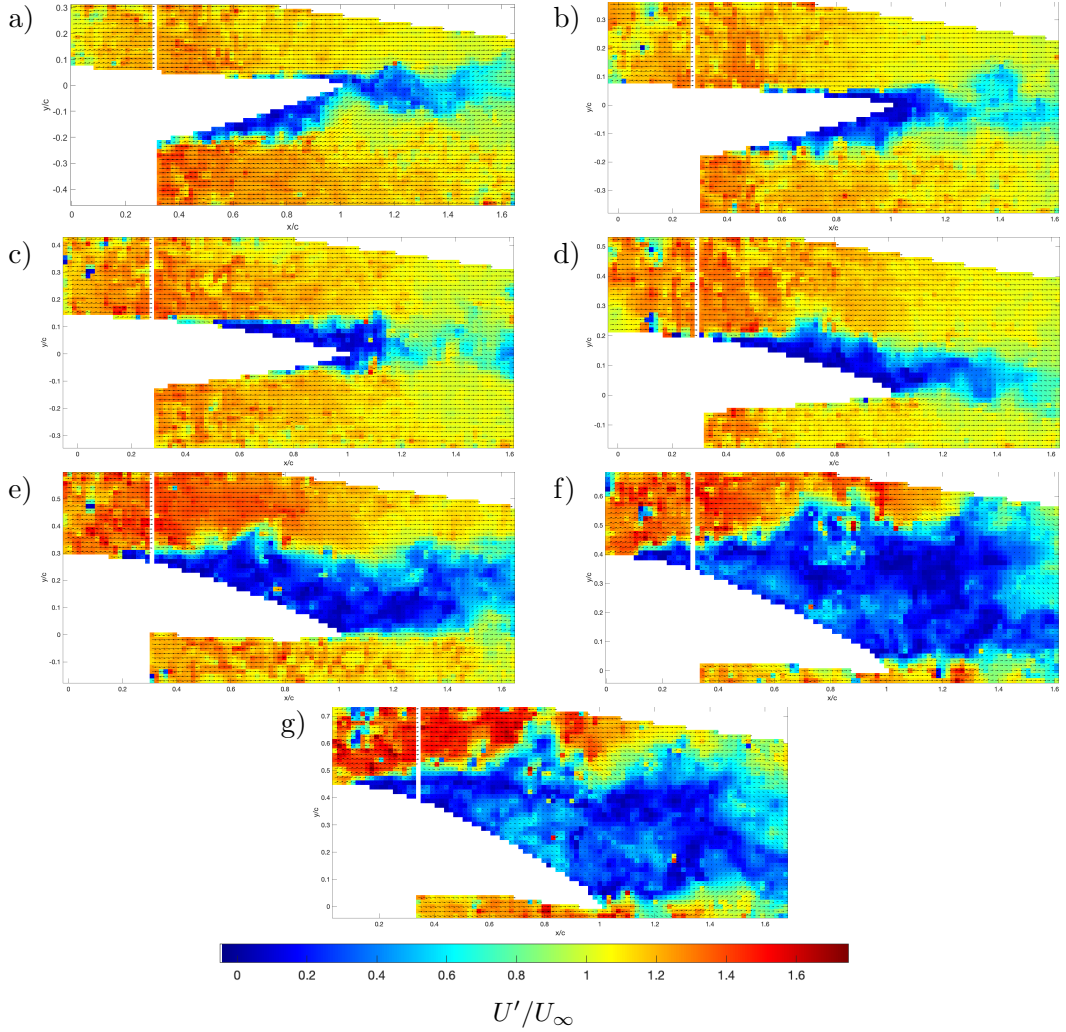


Figure 7: Randomly chosen instantaneous flow velocity vectors and coloured magnitude as a fraction of the freestream velocity around a NACA 0020 aerofoil at $Re_c = 19.6 \times 10^3$ at (a) $\alpha = -9^\circ$ (b) $\alpha = -5^\circ$ (c) $\alpha = 0^\circ$ (d) $\alpha = 4^\circ$ (e) $\alpha = 10^\circ$ (f) $\alpha = 16^\circ$ (g) $\alpha = 19^\circ$. $(\frac{x}{c}, \frac{y}{c}) = (1, 0)$ is set at the trailing edge of the aerofoil. White sections indicate where masks were drawn over the aerofoil, the laser sheet shadow, and where not enough particles were visible.

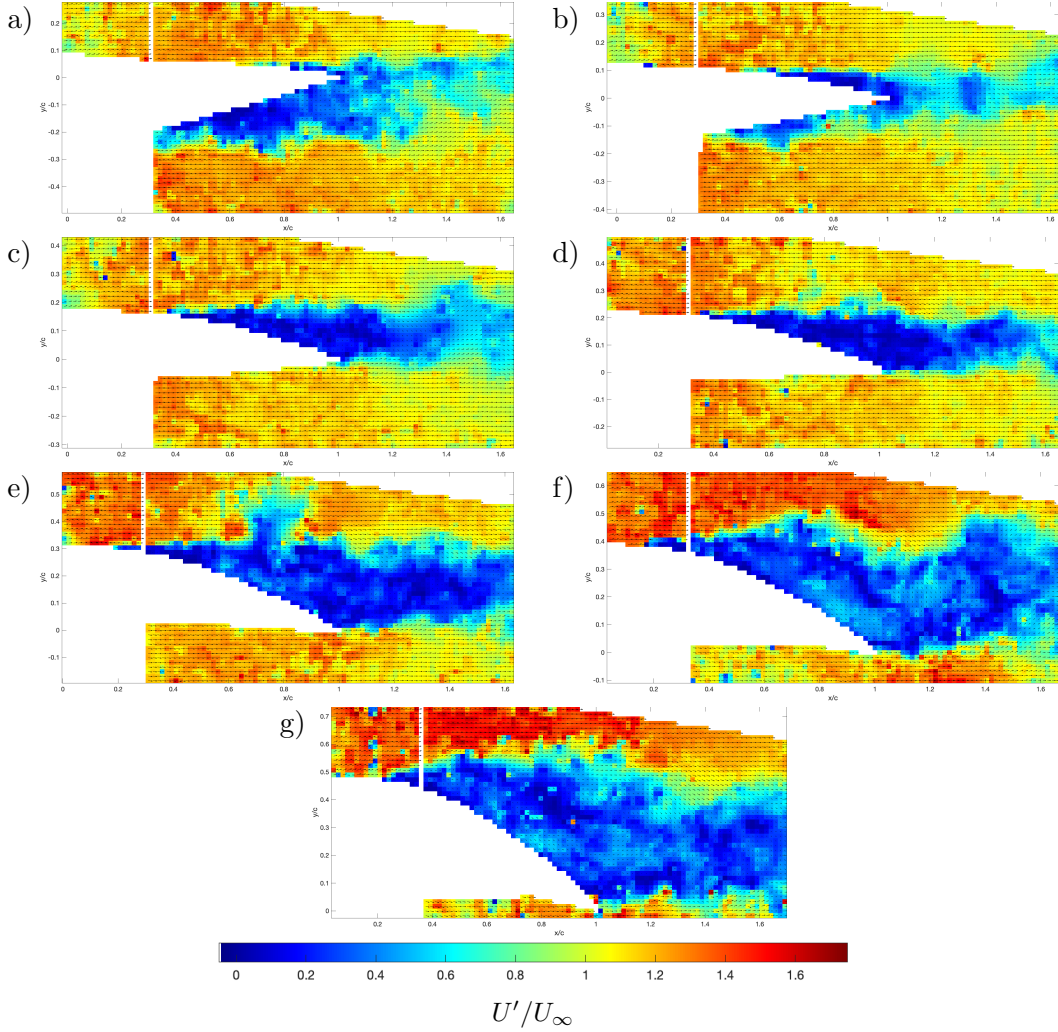


Figure 8: Randomly chosen instantaneous flow velocity vectors and coloured magnitude as a fraction of the freestream velocity around a NACA 4420 aerofoil at $Re_c = 19.6 \times 10^3$ at (a) $\alpha = -10^\circ$ (b) $\alpha = -5^\circ$ (c) $\alpha = 1^\circ$ (d) $\alpha = 3^\circ$ (e) $\alpha = 10^\circ$ (f) $\alpha = 15^\circ$ (g) $\alpha = 20^\circ$. $(\frac{x}{c}, \frac{y}{c}) = (1, 0)$ is set at the trailing edge of the aerofoil. White sections indicate where masks were drawn over the aerofoil, the laser sheet shadow, and where not enough particles were visible.

the angle of attack increases $\alpha = 0^\circ$ and decreases in speed below the aerofoil.

4.4 Turbulence Kinetic Energy

4.4.1 NACA 0020 Symmetric Aerofoil

In the top left corner of the all graphs along with a distinctive vertical line at all angles of attack the turbulence kinetic energy is significantly higher than the surrounding cells for the NACA 0020 aerofoil (Figure 9). The turbulence kinetic energy at $\alpha \leq 10^\circ$ is at a significantly lower magnitude than that of $\alpha = 15^\circ, 20^\circ$. At $\alpha = -9^\circ$, we saw a plume of turbulence emanated upwards from approximately $\frac{x}{c} = 0.3$ below the aerofoil and a small amount near the trailing edge above the aerofoil (Figure 9a). At $\alpha = -5^\circ$, the magnitude of the turbulence kinetic energy is much lower and emanates from $\frac{x}{c} \approx 0.5$ below the aerofoil, but farther forward above the aerofoil than $\alpha = -9^\circ$ at $\frac{x}{c} \approx 0.6 - 0.7$ (Figure 9b). At $\alpha = 0^\circ$, we saw the turbulence kinetic energy of approximately the same magnitude emanated above and below the aerofoil almost horizontally (and almost converged) from $\frac{x}{c} \approx 0.4$ and right before the trailing edge respectively (Figure 9c). At $\alpha = 4^\circ$, we saw one cell at approximately $\frac{x}{c} = 0.2$ have extremely high turbulence followed by a plume of turbulence emanated slightly downwards exclusively from above the aerofoil (Figure 9d). At $\alpha = 10^\circ$, we see the magnitude of turbulence increase, with a plume emanated upwards from $\frac{x}{c} \approx 0.2$ arced downwards and from the trailing edge (Figure 9e). The plumes described so far have generally circumscribed a region of slightly higher magnitude turbulent flow than the surrounding flow. At $\alpha = 16^\circ, 19^\circ$, the plume of turbulent flow had magnitudes of around $0.08 - 0.12 \text{ J/kg}$ (Figure 9f & 9g) unlike shallower angles of attack which generally had a maximum of around 0.08 J/kg . Furthermore, these plumes are much larger in area and both emanate upwards from $\frac{x}{c} \approx 0.1$ formed a large downwards arc and at the trailing edge. These turbulent plumes also circumscribe an area of a higher variation in turbulence kinetic energy.

4.4.2 NACA 4420 Cambered Aerofoil

Similarly for the NACA 4420 aerofoil we again have cells in the top left corner of the all graphs, along with a distinctive vertical line at all angles of attack, whose turbulence kinetic energy is significantly higher than the surrounding cells (Figure 10). We also still had turbulent plumes that circumscribed an area of slightly turbulent flow. At $\alpha = -10^\circ$, the plume emanates from the masked area below the aerofoil arced upwards and a smaller one from $\frac{x}{c} \approx 0.8$ above the aerofoil (Figure 10a). Save for a few cells, the region of turbulence kinetic energy is not surrounded by plumes of turbulent flow for $\alpha = -5^\circ$ and $\alpha = 1^\circ$ (Figure 10b & 10c). The turbulent region for the former starts near the trailing edge above the aerofoil and $\frac{x}{c} \approx 0.3$ below the aerofoil, whilst for the latter, the region starts at $\frac{x}{c} \approx 0.4$ above the aerofoil and

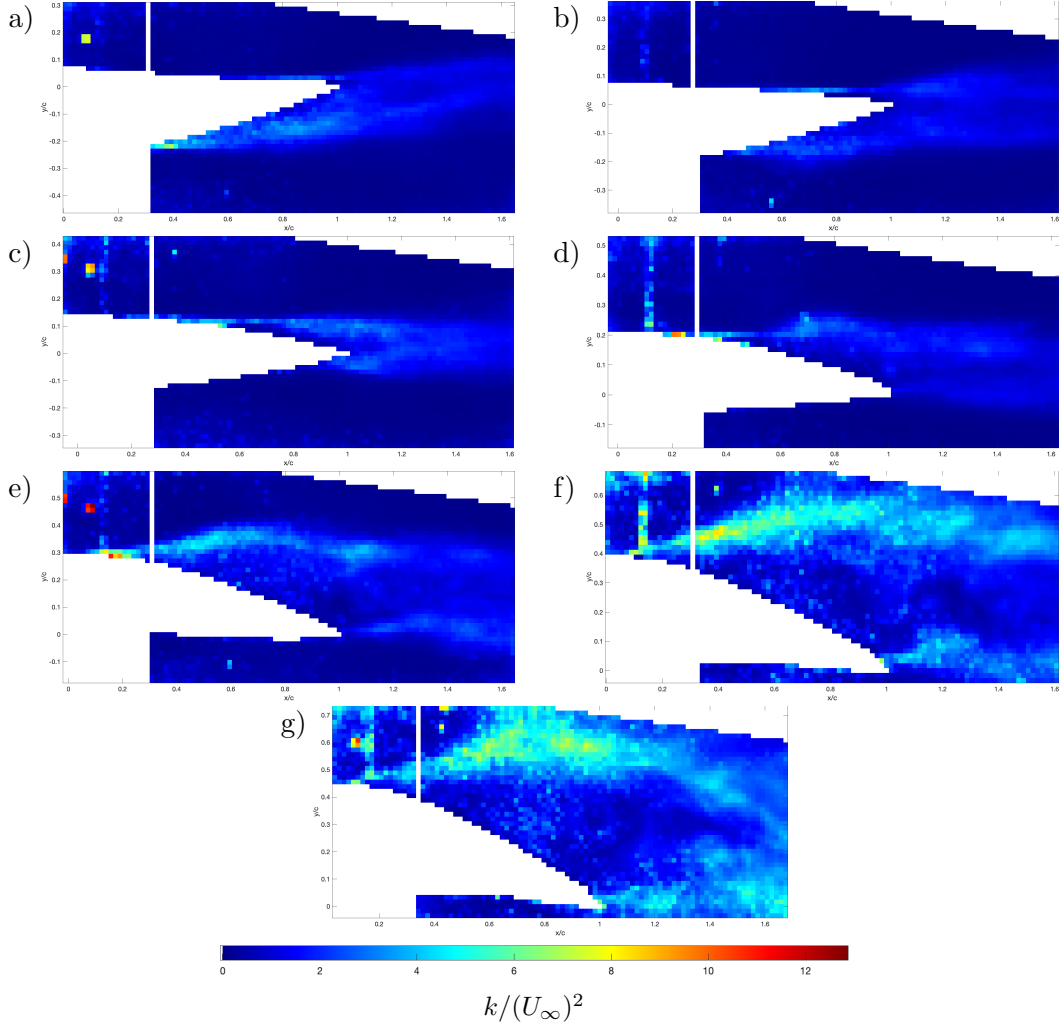


Figure 9: Turbulence kinetic energy of the flow around a NACA 0020 aerofoil as a fraction of $(U_\infty)^2$ at $Re_c = 19.6 \times 10^3$ at (a) $\alpha = -9^\circ$ (b) $\alpha = -5^\circ$ (c) $\alpha = 0^\circ$ (d) $\alpha = 4^\circ$ (e) $\alpha = 10^\circ$ (f) $\alpha = 16^\circ$ (g) $\alpha = 19^\circ$. $(\frac{x}{c}, \frac{y}{c}) = (1, 0)$ is set at the trailing edge of the aerofoil. White sections indicate where masks were drawn over the aerofoil, the laser sheet shadow, and where not enough particles were visible.

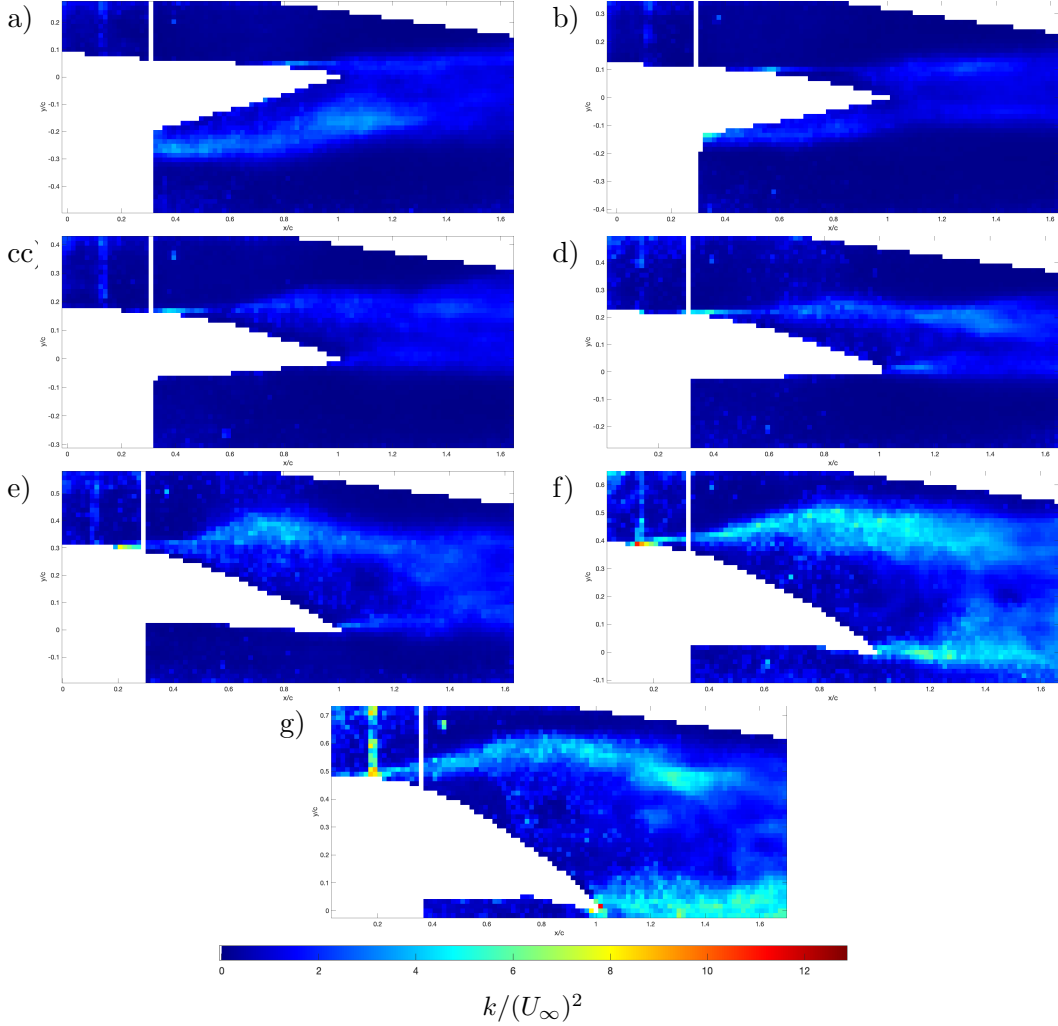


Figure 10: Turbulence kinetic energy of the flow around a NACA 4420 aerofoil as a fraction of $(U_\infty)^2$ at $Re_c = 19.6 \times 10^3$ at (a) $\alpha = -10^\circ$ (b) $\alpha = -5^\circ$ (c) $\alpha = 1^\circ$ (d) $\alpha = 3^\circ$ (e) $\alpha = 10^\circ$ (f) $\alpha = 15^\circ$ (g) $\alpha = 20^\circ$. $(\frac{x}{c}, \frac{y}{c}) = (1, 0)$ is set at the trailing edge of the aerofoil. White sections indicate where masks were drawn over the aerofoil, the laser sheet shadow, and where not enough particles were visible.

near the trailing edge below the aerofoil. The turbulent plume comes back at $\alpha = 3^\circ$ emanated from $\frac{x}{c} \approx 0.3$ above the aerofoil and at the trailing edge (Figure 10d). At $\alpha = 15^\circ$, the turbulent plume above the aerofoil starts to expand in area, it emanated up from $\frac{x}{c} \approx 0.2$ and is a larger amount of energy; the other plume emanates from the trailing edge (Figure 10e). These circumscribe a region with a slightly large amount of variation in turbulence kinetic energy. At $\alpha = 15^\circ$ and $\alpha = 20^\circ$, we saw a large plume of turbulence kinetic energy reaching magnitudes of approximately $0.08 - 0.09 \text{ J/kg}$, it emanated upwards then arced downwards, furthermore, unlike shallower angles of attack, a similarly large plume of turbulent flow of approximate magnitude also emanated from the trailing edge (Figure 10f & 10g). These plumes surrounded an area with very large variance in turbulence kinetic energy.

4.5 Errors

Firstly, at zero angle of attack, it is expected that a symmetric aerofoil would produce equal flows on both sides of the aerofoil. However this does not seem to be the case, as seen in Figure 5c, the region of low velocity has a larger area above the aerofoil than below. This may be due to incorrect placement of the aerofoil angle of attack, which may cause large differences in the flow (Burgmann and Schröder, 2008), as there is a random error of $\pm 0.5^\circ$ with the protractor; it may be due to the placement of the camera angled above the aerofoil; or it may be due to a systematic error in the angle of the freestream. These sources of errors must be acknowledged in all other collected data. Moreover, many of the average velocity and turbulence kinetic energy results (Figures 5, 6, 9, 10) show distinctive splotches or vertical lines that have a larger magnitude than the surrounding above the aerofoil near the leading edge, this is due to a systematic error from the data processing software interpreting the stationary mount edge as particles. Furthermore, in front of that line the speed in the average and instantaneous velocity plots generally decrease dramatically (Figures 5-8), which is likely to do with insufficient light in that area (as the laser sheet comes from the rear). Finally, Figures 7-8 show that despite an attempt to minimise error through post-processing, many erroneous data are still extant and propagated in calculations of averages and turbulence kinetic energy.

5 Discussion

5.1 Lift and Drag

Due to the decreasing strength of the laser further upstream and the shadow cast by the aerofoil, there were not enough particles that scattered enough light to be picked up strongly by the camera sensor in some areas around the aerofoil. This means that it is not possible to calculate an exact number for circulation and therefore lift, as it requires a sum of velocities along a closed curve around an aerofoil. We therefore relied on qualitative assessments of quantitative data to form our analysis.

We found that a symmetric aerofoil makes the flow behave differently than a cambered aerofoil. Furthermore, the flow behaves differently at different angles of attack. As discussed in Section 2.2.1, an aerofoil changes the direction of a packet of fluid in order to create lift. We can see these differences by looking at the average velocity field (Figures 5-6). Moreover, we can see from instantaneous velocity fields large differences in flow velocities at different points of the flow field at different angles of attack (Figures 7-8). At negative angles of attack, the symmetric aerofoils were able to redirect the streamlines upwards much more than the cambered aerofoils. In addition, the fluid speed below both aerofoils (disregarding the backflow) is much higher than that above, meaning the pressure below the aerofoils is lower than that above. However, the symmetric aerofoil has faster flow below the aerofoil than the cambered aerofoil, which again shows that at negative angles of attack, the symmetric aerofoils have more negative lift (or downforce) than the cambered aerofoil.

At zero angle of attack, the cambered aerofoil is able to redirect the flow above downwards, whereas the symmetric aerofoil approximately redirects the streamlines above and below equally downwards and upwards respectively. Furthermore, disregarding the backflow, the cambered aerofoil has slightly higher speed flow above the aerofoil than below as opposed to the symmetric aerofoil which has velocity of equal magnitude in similarly shaped clusters above and below the aerofoil. This means that the cambered aerofoil is likely providing a small amount of lift compared to no lift for the symmetric aerofoil.

At lower positive angles of attack, although both types of aerofoils are able to redirect flow downwards above the aerofoil, it is hard to tell which one is able to provide more lift through qualitative analysis of the figures. Although it is expected that the cambered aerofoil should generate greater lift, the separation occurs earlier along the aerofoil and creates a larger region of separation. Nonetheless, we saw that there are significant regions above the aerofoils that have faster speeds than below the aerofoils at these lower positive angles of attack signifying lift in the upwards direction. However, at large positive angles of attack, despite a region above the aerofoil with extremely high speed flow, both aerofoils are unable to redirect fluid flow downwards directly above the aerofoil (it does so in the wake). This occurs at around $\alpha = 10^\circ - 15^\circ$, which means that the aerofoil likely stalled at these angles.

For drag, as mentioned in Section 2.2.2, when encountering significant adverse pressure gradient, the thin boundary layer will begin to backflow and recirculate, causing the boundary layer to separate, creating a region of low speed flow. These regions grew in size as the aerofoils deviated from $\alpha = 0^\circ$, this means that, as expected, there is more pressure drag as angle of attack deviates from 0° .

5.2 Turbulence and Coherent Structures

The nature and structures created by the backflow is what makes the aerofoils in low Reynolds number flow interesting. The plumes where the turbulence kinetic energy is highest (Figures 9-10) tends to match the boundaries in the average flow fields in Figures 5-6 between the slow moving backflow region and the fast moving streamlined flow. Since the turbulence is occurring at the interface between two regions, it signifies that the initial prediction of Kelvin-Helmhotz instabilities is likely to be correct. Furthermore, the instantaneous flows show peaks and troughs that signify signs of coherent structures.

However, at higher angles of attack we saw that the turbulent plumes occupied a much larger area at higher magnitudes of k from both the boundary layer separation at the trailing edge from the bottom surface and from separation near the leading edge from the upper surface. In fact, combining the data from turbulence kinetic energy and the instantaneous flows, the recirculatory areas of the aerofoils at these higher angles of attack seem to have more fluctuation in the wake of both the upper and bottom surface, and less structure. This shows that both aerofoils start to behave more like blunt bodies at higher angles of attack.

6 Conclusion

This experiment confirms the prevailing theories on the differences between symmetric and cambered aerofoils at different angles of attack in low Reynolds number flow. Although Yarusevych et al. (2009) still mentions that there are a lot of intricacies in resolving the exact nature of turbulence in the flow of around an aerofoil in low Reynolds number flow. As there are no analytical solutions to the Navier-Stokes equations as of yet to describe this flow, and since current computing technology does not allow us to resolve small scale turbulence with CFD at a low cost (Spalart, 2000), it is imperative that we observe these flows in further experimental fluid dynamics to investigate these situations. Furthermore, Burgmann and Schröder (2008) states that the vortices formed in the recirculatory regions of aerofoils in low Reynolds number flow are three dimensional and time dependent both factors were not investigated thoroughly in this experiment. There is therefore still much to observe and understand that this analysis did not cover.

Experimental observations of fluid dynamics not only lets us see the flow field directly but also allows us to confirm or contradict results from CFD simulations so that future CFD programmes could be improved. Both experimental and CFD results of fluid flow around aerofoils and other objects helps us engineer better performing and more efficient vehicles and machines. This can mean different things for different applications but will many times involve reducing fossil fuel consumption, decreasing our impact on human induced global climate change. More funda-

mentally, however, observing fluid flow allows us to gain a deeper insight into the workings of fluid dynamics, and perhaps one day unravel the mystery surrounding the still elusive nature of turbulence.

References

- Adrian, R. J. and Westerweel, J. (2011). *Particle Image Velocimetry*. Cambridge University Press.
- Anderson, J. D. (1995). *Computational Fluid Dynamics: The Basics with Applications*. McGraw-Hill series in mechanical engineering. McGraw-Hill, New York.
- Anderson, J. D. (2011). *Fundamentals of Aerodynamics*. Anderson series. McGraw-Hill, New York, 5th ed edition. OCLC: ocn463634144.
- Anderson, J. D. (2016). *Introduction to Flight*. McGraw-Hill Education, New York. OCLC: 968929906.
- Babinsky, H. (2003). How do wings work? *Physics Education*, 38(6):497.
- Burgmann, S. and Schröder, W. (2008). Investigation of the vortex induced unsteadiness of a separation bubble via time-resolved and scanning PIV measurements. *Experiments in Fluids*, 45(4):675.
- Davidson, P. A. (2004). *Turbulence : An Introduction for Scientists and Engineers*. OUP Oxford.
- Euler, L. (1757). Principes généraux du mouvement des fluides. *Mémoires de l'Académie des Sciences de Berlin*, pages 274–315.
- Evonik (2015). VESTOSINT® 2157 natural color - Product Information. Retrieved from <https://www.vestosint.com/product/peek-industrial/downloads/pi-vestosint-2157-natural-en.pdf>.
- Friedlander, S. and Lipton-Lifschitz, A. (2003). Localized Instabilities in Fluids. In *Handbook of Mathematical Fluid Dynamics*, volume 2, pages 289–354. Elsevier.
- Hsiao, F.-B., Liu, C.-F., and Tang, Z. (1989). Aerodynamic performance and flow structure studies of a low Reynoldsnumber airfoil. *AIAA Journal*, 27(2):129–137.
- Huang, R. F., Wu, J. Y., Jeng, J. H., and Chen, R. C. (2001). Surface flow and vortex shedding of an impulsively started wing. *Journal of Fluid Mechanics*, 441:265–292.
- ICAO (2010). ICAO Environmental Report. Retrieved from <https://www.icao.int/environmental-protection/Documents/EnvironmentReport-2010/>.
- International Towing Tank Conference (2011). ITTC - Recommended Procedures: Fresh Water and Seawater Properties. Retrieved from <https://ittc.info/media/4048/75-02-01-03.pdf>.
- Jacobs, E. N., Kenneth, W., and Pinkerton, R. M. (1933). The characteristics of 78 related airfoil sections from tests in the variable-density wind tunnel. Technical Report 460, NACA.

- JAI (2020). Go Series GO-2400C-USB compact 2.35 MP area scan camera. Retrieved from <https://www.jai.com/products/go-2400c-usb>.
- Kundu, P. K., Cohen, I. M., and Dowling, D. R. (2012). *Fluid mechanics*. Academic Press, Waltham, MA, 5th ed edition.
- Ladson, C. L. B. (1975). Development of a computer program to obtain ordinates for NACA 4-digit, 4-digit modified, 5-digit, and 16 series airfoils. Technical report, NASA.
- Lee, J., Lukachko, S., Waitz, I., and Schafer, A. (2001). Historical and future trends in aircraft performance, cost, and emissions. *Annual Review of Energy and the Environment*, 26.
- Raffel, M., Willert, C. E., Scarano, F., Kähler, C. J., Wereley, S. T., and Kompenhans, J. (2018). *Particle Image Velocimetry : A Practical Guide*, volume Third edition. Springer, Cham.
- Resnick, R., Walker, J., and Halliday, D. (1988). *Fundamentals of physics*, volume 1. John Wiley Hoboken.
- Singh, V. and Sharma, S. K. (2015). Fuel consumption optimization in air transport: a review, classification, critique, simple meta-analysis, and future research implications. *European Transport Research Review*, 7(2):12.
- Solarfilm Sales Ltd (2020). Solarfilm Sales Ltd. Retrieved from <https://solarfilm.co.uk>.
- Spalart, P. (2000). Strategies for turbulence modelling and simulations. *International Journal of Heat and Fluid Flow*, 21(3):252–263.
- Tanner, R. I. and Walters, K. (1998). The Growing Years Before 1945. In *Rheology: An Historical Perspective*, volume 7 of *Rheology Series*, pages 25 – 42. Elsevier. ISSN: 0169-3107.
- Thielicke, W. (2019). PIVlab - particle image velocimetry (PIV) tool (version 2.31). Retrieved from <https://uk.mathworks.com/matlabcentral/fileexchange/27659-pivlab-particle-image-velocimetry-piv-tool>.
- Thorlabs (2011). Thorlabs - CPS532 Collimated Laser-Diode-Pumped DPSS Laser Module, 532 nm, 4.5 mW, Round Beam, Ø11 mm Housing. Retrieved from <https://www.thorlabs.com/thorproduct.cfm?partnumber=CPS532>.
- Watmuff, J. H. (1999). Evolution of a wave packet into vortex loops in a laminar separation bubble. *Journal of Fluid Mechanics*, 397:119–169.
- Westerweel, J., Elsinga, G. E., and Adrian, R. J. (2013). Particle Image Velocimetry for Complex and Turbulent Flows. *Annual Review of Fluid Mechanics*, 45(1):409–436.

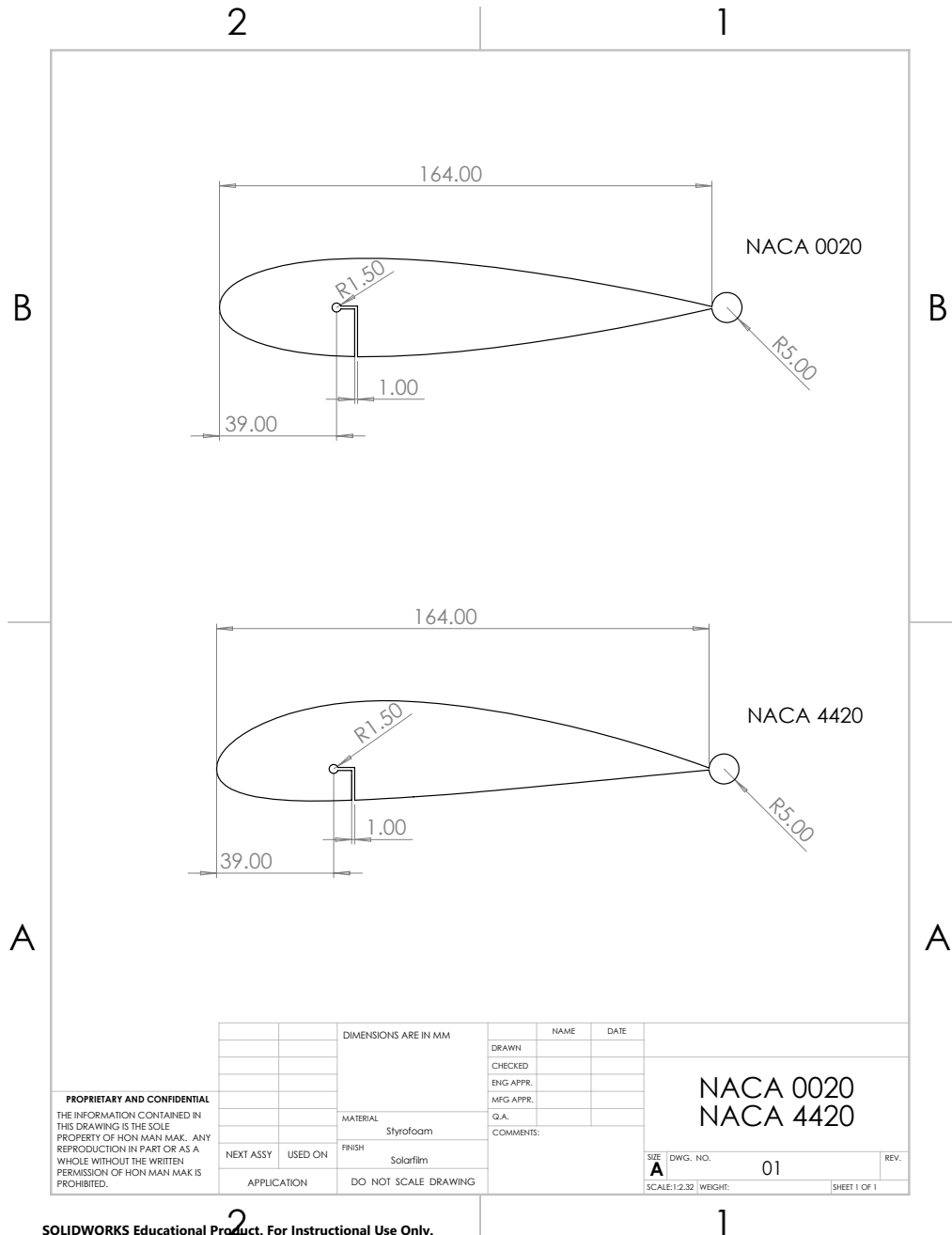
White, F. M. (2009). *Fluid mechanics*. McGraw-Hill series in mechanical engineering.
McGraw-Hill, New York, NY, 7th ed edition.

Yarusevych, S. and Boutilier, M. S. H. (2011). Vortex Shedding of an Airfoil at Low
Reynolds Numbers. *AIAA Journal*, 49(10):2221–2227.

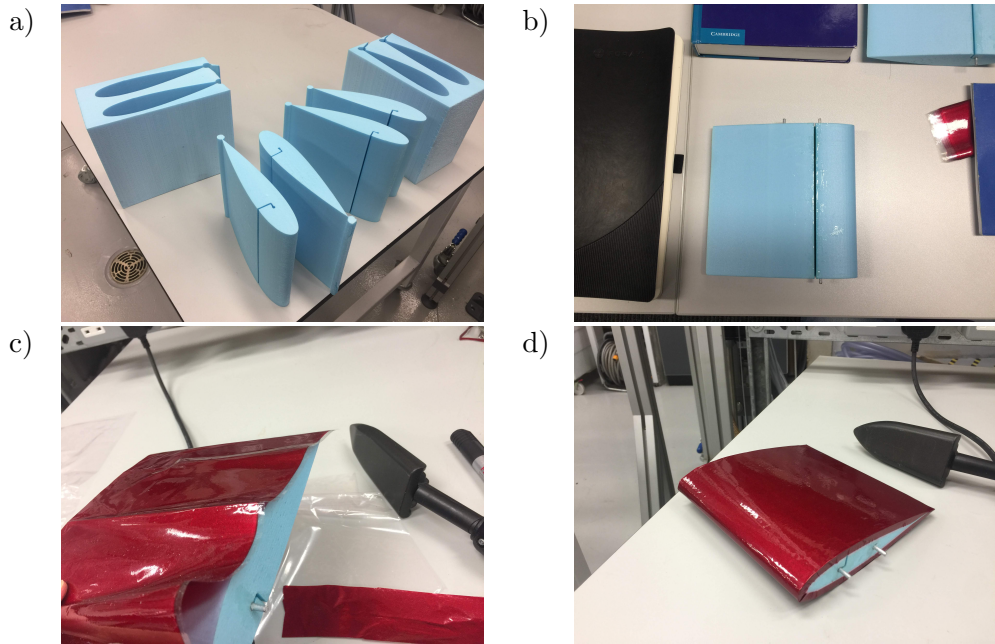
Yarusevych, S., Sullivan, P. E., and Kawall, J. G. (2009). On vortex shedding from
an airfoil in low-Reynolds-number flows. *Journal of Fluid Mechanics*, 632:245–271.

A Aerofoil Models

A.1 Styrofoam Cut Engineering Drawings



A.2 Manufacturing Process



B MATLAB Code

B.1 Freestream Data Processing

```

1 load('PIVlab.mat')
2
3 vel = cell(length(u_filtered),3);
4 % get velocities with masked picture
5 for i = 1:length(u_filtered)
6     vel(i,1) = {times(u_filtered{i},typevector_original{i})};
7     vel(i,2) = {times(v_filtered{i},typevector_original{i})};
8     vel(i,3) = {sqrt(times(vel{i,1},vel{i,1})+times(vel{i,2},vel{i,2}))};
9 end
10
11 % delete error velocity matrices
12 vel(118,:) = [];
13 vel(110,:) = [];
14 vel(107,:) = [];
15 vel(103,:) = [];
16 vel(100,:) = [];
17
18 % find average velocity matrix
19
20 velmean = zeros(size(vel{1,1}));
21 for i = 1:length(vel)
22     velmean = velmean + vel{i,3};
23 end
24 velmean = velmean/length(vel);
25
26 % set masked section as NaN

```

```

27 velmean(velmean == 0) = NaN;
28
29 % output median value in average velocity matrix
30 disp(nanmedian(velmean, 'all'))

```

B.2 Aerofoil Flow Field Data Processing

```

1 [~, dir] = xlsread('directory.xlsx');
2 errdir = readmatrix('piverror.xlsx');
3
4 % declare cells
5 err = cell(14,4);
6 v_i = cell(14,4);
7 velmean = cell(14,4);
8 turb_ke = cell(14,4);
9 X = cell(14,4);
10 Y = cell(14,4);
11
12 % store error frames in 14x4 cell
13 for i = 1:14
14     err(i,1) = {errdir(:,i)};
15 end
16 for i = 15:28
17     err(i-14,2) = {errdir(:,i)};
18 end
19 for i = 29:42
20     err(i-28,3) = {errdir(:,i)};
21 end
22 for i = 43:56
23     err(i-42,4) = {errdir(:,i)};
24 end
25
26 % run data calculations for mean velocities and turbulence KE
27 for j = 1:14
28     for k = 1:4
29         % get data in MATLAB workspace
30         load(dir{j,k})
31         vel = cell(length(u_filtered),3);
32         % get velocities with masked picture
33         for i = 1:length(u_filtered)
34             vel(i,1) = {times(u_filtered{i},typevector_original{i})/.12};
35             vel(i,2) = {times(v_filtered{i},typevector_original{i})/.12};
36             vel(i,3) = {sqrt(times(vel{i,1},vel{i,1})+times(vel{i,2},vel{i,2}))};
37         end
38
39         % store mask for figure generation
40         mask(j,k) = {typevector_original{1}};
41
42         % delete error velocity matrices
43         m = 1;
44         for i = 1:length(vel)
45             if err{j,k}(i,1) == 1
46                 vel(m,:) = [];
47             else
48                 % if matrix is deleted the index i is now out of sync
49                 m = m + 1;
50             end
51         end
52         v_i(j,k) = {vel};

```

```

53
54     mean_tmp = cell(1,3);
55     % find average velocities
56     for m = 1:3
57         mean_tmp(m) = {zeros(size(vel{1,1}))};
58         for i = 1:length(vel)
59             mean_tmp{m} = mean_tmp{m} + vel{i,m};
60         end
61         mean_tmp{m} = mean_tmp{m}/length(vel);
62     end
63     velmean(j,k) = {mean_tmp};
64     clear mean_temp
65
66     var = cell(1,2);
67     diff = cell(length(vel),2);
68     % find mean variance
69     for m = 1:2
70         var(m) = {zeros(size(vel{1,1}))};
71         for i = 1:length(vel)
72             diff(i,m) = {vel{i,m}-velmean{j,k}{1,m}};
73             var{m} = var{m} + times(diff{i,m},diff{i,m});
74         end
75         var{m} = var{m}/length(vel);
76     end
77     % calculate turb KE from variance and non-dimensionalise
78     turb_ke(j,k) = {((var{1}+var{2})/2)/(.12^2)};
79     clear diff
80     clear var
81
82     % find where x/c = 1 by looking for the first zero square from the
83     % right thirteen squares down
84     a = 0;
85     n = size(typevector_original{1,1},2);
86     while true
87         for i = 13:size(typevector_original{1,1},1)
88             if typevector_original{1,1}(i,n) == 0
89                 a = i;
90             end
91         end
92         if a ~= 0
93             break
94         else
95             n = n-1;
96         end
97     end
98
99     % store non-dimensional axes (lengthscale)
100    X(j,k) = {(x{1,1})(1,:)-(x{1,1})(1,n))/164+1};
101    Y(j,k) = {-(y{1,1})(:,1)-(y{1,1})(a,1))/164};
102 end
103 end

```

B.3 Figure Creation

```

1 % if 0 = worse aoa; if 2 = produces worse picture
2 goodaoa = [0 1 1 0;0 2 2 0;2 0 1 0;1 0 2 0;0 1 2 0;0 2 1 0;2 0 0 2;...
3     1 0 0 1;0 1 0 2;0 2 0 1;1 0 0 2;2 0 0 1;0 2 2 0;0 1 1 0];
4
5 % create colorbar
6 cmap = jet(256);

```

```

7  cmap(1,:) = 1;
8
9 % mean velocity max range
10 vmax = 0;
11 for j = 1:14
12     for k = 4:4
13         localvmax = max(velmean{j,k}{1,3},[],'all');
14         if localvmax > vmax && goodaoa(j,k) == 1
15             vmax = localvmax;
16         end
17     end
18 end
19
20 % mean velocity plot
21 for j = 1:14
22     for k = 1:4
23         if goodaoa(j,k) == 1
24             % colour map
25             imagesc(X{j,k},Y{j,k},velmean{j,k}{1,3},[0,vmax]);
26             colormap(cmap);
27             % c = colorbar('southoutside') % for outputting colorbar
28             hold on
29             % streamlines
30             h = streamslice(X{j,k},Y{j,k},velmean{j,k}{1,1},-velmean{j,k}
31                             ){1,2});
32             set(h, 'Color', [0 0 0] );
33             % figure styling parameters
34             set(gca,'YDir','normal');
35             xlabel('x/c')
36             ylabel('y/c')
37             set(gca,'FontSize',12);
38             set(gcf, 'Position', [0 0 900 435]);
39             ax = gca;
40             outerpos = ax.OuterPosition;
41             ti = ax.TightInset;
42             left = outerpos(1) + ti(1);
43             bottom = outerpos(2) + ti(2);
44             ax_width = outerpos(3) - ti(1) - ti(3);
45             ax_height = outerpos(4) - ti(2) - ti(4);
46             ax.Position = [left bottom ax_width ax_height];
47
48             %save figure
49             saveas(gcf,filename(j,k,''));
50             hold off
51             clf
52         end
53     end
54
55 % instantaneous velocity max range
56 vimax = 0;
57 for j = 1:14
58     for k = 1:4
59         for i = 1:length(v_i{j,k})
60             localvimax = max(v_i{j,k}{i,3},[],'all');
61             if localvimax > vimax && goodaoa(j,k) == 1
62                 vimax = localvimax;
63             end
64         end
65     end

```

```

66 end
67
68 framestore = zeros(14,4);
69 % instantaneous velocity plot
70 for j = 1:14
71     for k = 1:4
72         if goodaoa(j,k) == 1
73             % random number for frame selection
74             inst = randi([1 length(v_i{j,k})]);
75             % store number for future reference
76             framestore(j,k) = inst;
77
78             % change masks (i.e. zero cells) to -0.05 for better visuals
79             for m = 1:size(v_i{j,k}{inst,3},1)
80                 for n = 1:size(v_i{j,k}{inst,3},2)
81                     if mask{j,k}{m,n} == 0
82                         v_i{j,k}{inst,3}(m,n) = -0.05;
83                     end
84                 end
85             end
86
87             % colour map
88             imagesc(X{j,k},Y{j,k},v_i{j,k}{inst,3},[-0.05,vimax])
89             colormap(cmap);
90             % c = colorbar('southoutside'); % for outputting colorbar
91             hold on
92             % velocity vectors
93             h = quiver(X{j,k},Y{j,k},v_i{j,k}{inst,1},-v_i{j,k}{inst,2});
94             set(h, 'Color', [0 0 0]);
95             % figure styling parameters
96             set(gca,'YDir','normal');
97             xlabel('x/c')
98             ylabel('y/c')
99             set(gca,'FontSize',12);
100            set(gcf, 'Position', [0 0 900 435])
101            ax = gca;
102            outerpos = ax.OuterPosition;
103            ti = ax.TightInset;
104            left = outerpos(1) + ti(1);
105            bottom = outerpos(2) + ti(2);
106            ax_width = outerpos(3) - ti(1) - ti(3);
107            ax_height = outerpos(4) - ti(2) - ti(4);
108            ax.Position = [left bottom ax_width ax_height];
109
110            %save figure
111            saveas(gcf,filename(j,k,'in'));
112            hold off
113            clf
114        end
115    end
116 end
117
118 % turbulence kinetic energy max range
119 turbmax = 0;
120 for j = 1:14
121     for k = 1:4
122         localtmax = max(turb_ke{j,k},[],'all');
123         if localtmax > turbmax && goodaoa(j,k) == 1
124             turbmax = localtmax;
125         end

```

```

126     end
127 end
128
129 % turbulence kinetic energy plot
130 for j = 1:14
131     for k = 1:4
132         if goodaoa(j,k) == 1
133             % change masks (i.e. zero cells) to negative for better visuals
134             for m = 1:size(turb_ke{j,k},1)
135                 for n = 1:size(turb_ke{j,k},2)
136                     if mask{j,k}(m,n) == 0
137                         turb_ke{j,k}(m,n) = -.05;
138                     end
139                 end
140             end
141             imagesc(X{j,k},Y{j,k},turb_ke{j,k},[-.05,turbmax])
142             colormap(cmap);
143             % c = colorbar('southoutside'); % for outputting colorbar
144             % figure styling parameters
145             set(gca,'YDir','normal');
146             xlabel('x/c')
147             ylabel('y/c')
148             set(gca,'FontSize',12);
149             set(gcf, 'Position', [0 0 900 435])
150             ax = gca;
151             outerpos = ax.OuterPosition;
152             ti = ax.TightInset;
153             left = outerpos(1) + ti(1);
154             bottom = outerpos(2) + ti(2);
155             ax_width = outerpos(3) - ti(1) - ti(3);
156             ax_height = outerpos(4) - ti(2) - ti(4);
157             ax.Position = [left bottom ax_width ax_height];
158
159             %save figure
160             saveas(gcf,filename(j,k,'tb'));
161             hold off
162             clf
163         end
164     end
165 end
166
167 % file naming function
168 function p = filename(trial,wingnum,figtype)
169     aoa = 5*ceil(trial/2-3);
170
171     if wingnum <= 2
172         wing = '0020';
173     else
174         wing = '4420';
175     end
176
177     if aoa < 0
178         p = sprintf('%s%s_n%_d.png',figtype,wing,-aoa);
179     else
180         p = sprintf('%s%s_%d.png',figtype,wing,aoa);
181     end
182 end

```